

Article

Sensitivity Enhancement of Silicon-on-Insulator CMOS MEMS Thermal Hot-Film Flow Sensors by Minimizing Membrane Conductive Heat Losses

Zahid Mehmood ^{1,2,*}, Ibraheem Haneef ², Syed Zeeshan Ali ³ and Florin Udrea ¹¹ Engineering Department, University of Cambridge, Cambridge CB3 0FA, UK; fu10000@hermes.cam.ac.uk² Institute of Avionics & Aeronautics, Air University, E-9, Islamabad 44000, Pakistan; ibraheem.haneef@mail.au.edu.pk³ AMS Sensors UK Ltd., Deanland House, 160 Cowley Road, Cambridge CB4 0DL, UK; Zeeshan.Ali@ams.com

* Correspondence: zahidm56@gmail.com; Tel.: +92-323-938-9698

Received: 7 March 2019; Accepted: 15 April 2019; Published: 18 April 2019



Abstract: Minimizing conductive heat losses in Micro-Electro-Mechanical-Systems (MEMS) thermal (hot-film) flow sensors is the key to minimize the sensors' power consumption and maximize their sensitivity. Through a comprehensive review of literature on MEMS thermal (calorimetric, time of flight, hot-film/hot-film) flow sensors published during the last two decades, we establish that for curtailing conductive heat losses in the sensors, researchers have either used low thermal conductivity substrate materials or, as a more effective solution, created low thermal conductivity membranes under the heaters/hot-films. However, no systematic experimental study exists that investigates the effect of membrane shape, membrane size, heater/hot-film length and *Membrane* (size) to *Heater* (hot-film length) *Ratio* (*MHR*) on sensors' conductive heat losses. Therefore, in this paper we have provided experimental evidence of dependence of conductive heat losses in membrane based MEMS hot-film flow sensors on *MHR* by using eight MEMS hot-film flow sensors, fabricated in a 1 μm silicon-on-insulator (SOI) CMOS foundry, that are thermally isolated by square and circular membranes. Experimental results demonstrate that: (a) thermal resistance of both square and circular membrane hot-film sensors increases with increasing *MHR*, and (b) conduction losses in square membrane based hot-film flow sensors are lower than the sensors having circular membrane. The difference (or gain) in thermal resistance of square membrane hot-film flow sensors viz-a-viz the sensors on circular membrane, however, decreases with increasing *MHR*. At *MHR* = 2, this difference is 5.2%, which reduces to 3.0% and 2.6% at *MHR* = 3 and *MHR* = 4, respectively. The study establishes that for membrane based SOI CMOS MEMS hot-film sensors, the optimum *MHR* is 3.35 for square membranes and 3.30 for circular membranes, beyond which the gain in sensors' thermal efficiency (thermal resistance) is not economical due to the associated sharp increase in the sensors' (membrane) size, which makes sensors more expensive as well as fragile. This paper hence, provides a key guideline to MEMS researchers for designing the square and circular membranes-supported micro-machined thermal (hot-film) flow sensors that are thermally most-efficient, mechanically robust and economically viable.

Keywords: MEMS thermal flow sensors; review; conduction losses; heater/hot-film; membrane shape; membrane to heater ratio; silicon-on-insulator (SOI); complementary metal oxide semiconductor (CMOS)

1. Introduction

Flow sensors are extensively used for flow measurements in diverse applications in different fields including aerospace [1–6], automotive [7], biomedical [8–11], environmental [12–17], hydrodynamics [18]

and the chemical and process industries [19]. They can be broadly classified as either non-thermal or thermal [20].

Non-thermal flow sensors can be grouped, as per their transduction scheme, into differential pressure-based, lift force-based, cantilever deflection-based and resonating frequency-based. A comprehensive review of these non-thermal flow sensors is presented by Wang et al. [21]. Thermal flow sensors, on the other hand, use temperature as the main measurand parameter. State of the art reviews of these sensors can be found in [20,21]. These have been investigated extensively because of their structural simplicity (no moving parts) and robustness, easy electrical interface, high temporal and spatial resolution, low cost and high reliability when mass fabricated using silicon technology [22,23]. According to their measurement techniques, thermal flow sensors can be segregated into three main types (or configurations): (a) calorimetric flow sensors [3,5,6,15,17,24–58], (b) time of flight (TOF) flow sensors [36,59–62] and (c) hot-wire (HW)/hot-film(HF)flow sensors [4,5,8–11,13,18,22,23,27,34,36,42,50,63–115].

Calorimetric thermal flow sensors are typically used to measure flow velocity [45,46,48,49], flow direction [17,47–49] and flow rate [51,52], whereas TOF thermal flow sensors are generally used to extract only flow velocity and flow rate [60,62]. Hot-film [11,71,77,110–112,114] and hot-wire [116] based thermal flow sensors have been used to measure flow velocity, mass/volume flow rate and fluidic wall shear stress.

Although calorimetric flow sensors have the highest sensitivity among the three types of thermal flow sensors, they however require at least two additional temperature sensors for extracting flow information [20,44]. In TOF thermal flow sensors, a thermal pulse, injected into a flow at point A, is detected downstream at point B. The total time taken by the pulse is then used for the flow measurements. This technique, however, has many drawbacks; i.e., requirement of injecting a thermal peak with enough energy to be detected downstream, rapid decay of peak due to longitudinal heat diffusion, conduction through the walls and Taylor dispersion [62]. Among these three measurement techniques, owing to its simple fabrication and implementation process, short response time and large flow measurement range, the hot-wire/hot-film configuration is the most widely investigated and adopted approach [58].

In the hot-wire/hot-film thermal flow sensors, a thin wire/film (often referred as hot-wire/hot-film or heater), placed over a low-thermal conductivity substrate or membrane, is heated above the ambient temperature. The amount of heat convected to the fluid passing over the hot-film/hot-wire is then transduced in terms of varying voltage of the heater to extract the flow information [20]. Since the fluid passing over the sensor only takes away heat through convective heat transfer, therefore, it is desirable to increase the convective heat transfer and reduce the conductive heat transfer [65] to the substrate.

Sensitivity and power consumption of all three types of thermal flow sensors (i.e., calorimetric, TOF, HW/HF) depends upon their ability to maximize convective heat transfer to the flow and minimize conduction losses to the substrate. To achieve this objective, researchers have resorted to two strategies: (a) use of low thermal conductivity substrate materials, and (b) thermal isolation of hot element by creating membranes under the heater/hot element.

In all three types of MEMS thermal flow sensors, the materials used as a substrate for minimizing conductive heat loss (from the heater/sensor to the substrate) are either ceramics or polymers. A comprehensive overview of ceramics and polymers used as substrate under different MEMS thermal flow sensors (heaters) is given in Tables 1 and 2, respectively.

Table 1. MEMS Thermal Flow Sensors Fabricated on Ceramic Substrates.

First Author, Year	[Ref]	Type	Sensor Material	Sensor Size ($l \times w \times t$, all in μm)	Substrate Material
Kuijk, 1995	[71]	TOF	Platinum	$300 \times 100 \times \text{NR}$	Glass
Tung, 2007	[99]	Hot-Film	MW CNT	$360 \times 90 \times \text{NR}$	Glass
Qu, 2008	[102]	Hot-Film	EG CNT	$1 \times 1 \times 0.1$	Glass
Zhu, 2015	[57]	Calorimetric	Platinum	$\text{NR} \times \text{NR} \times 0.2$	Silicon-in-Glass(SIG)
Makinwa, 2001	[15]	Calorimetric	Polysilicon	$2000 \times 200 \times \text{NR}$	Silicon/Ceramic for protection
Dominguez, 2008	[4]	Hot-Film	Platinum	$\text{NR} \times \text{NR} \times 0.07$	Silicon
*Makinwa, 2002	[17]	Calorimetric	Polysilicon	0.4 mm ² area	Silicon/Ceramic for protection
Matova, 2003	[47]	Calorimetric	P doped Silicon	$\text{NR} \times \text{NR} \times \text{NR}$	Silicon/Ceramic for protection
Kaltsas, 1999	[45]	Calorimetric	Polysilicon	$\text{NR} \times \text{NR} \times \text{NR}$	Porous Silicon
Kaltsas, 2002	[46]	Calorimetric	Polysilicon	$\text{NR} \times \text{NR} \times \text{NR}$	Porous Silicon
Stamatopoulos, 2008	[53]	Calorimetric	Polysilicon	$\text{NR} \times \text{NR} \times \text{NR}$	Porous Silicon
Sun, 2013	[112]	Hot-Film	Chromium/Platinum	$1500 \times 250 \times 0.17$	P-doped Silicon (Beam Material)
Wu, 2001	[95]	Hot-Film	Polysilicon	$\text{NR} \times \text{NR} \times \text{NR}$	SiN
Furjes, 2004	[48]	Calorimetric	Platinum	$100 \times 100 \times 1$	SiN
Dijkstra, 2008	[51]	Calorimetric	Platinum	$\text{NR} \times \text{NR} \times 0.2$	SiN
Wiegerink, 2009	[105]	Hot-Film	Aluminum	$\text{NR} \times \text{NR} \times \text{NR}$	SiN
Xiang, 2010	[55]	Calorimetric	Polysilicon	$\text{NR} \times \text{NR} \times 1$	Silicon
*Sun, 2007	[49]	Calorimetric	Polysilicon	$600 \times 60 \times \text{NR}$	Ceramic Al ₂ O ₃
Shen, 2010	[56]	Calorimetric	Platinum	$1000 \times 1000 \times 0.2$	Ceramic (Exact ceramic name not reported)
Miau, 2015	[94]	Hot-Film	Platinum	$200 \times 260 \times 0.1$	Polyimide

Legend for Tables 1–6. Hot-wire/Hot-film type thermal flow sensors; Calorimetric (Calori) type thermal flow sensors; Time of flight (TOF) type thermal flow sensors; CMOS Sensors; Sensors fabricated on Glass substrate; Sensors fabricated on Silicon substrate; Sensors fabricated on Porous Silicon substrate; Sensors fabricated on Other Ceramic substrate; Sensors fabricated on Silicon Nitride substrate/Membrane; Sensors fabricated on Silicon Oxide substrate/Membrane; Sensors fabricated on Polyimide substrate/Membrane; Sensors fabricated on Parylene substrate/Membrane; Sensors fabricated on Kapton substrate/Membrane; Sensors fabricated on Silicon Nitride/Silicon Oxide Membrane; SiN: Silicon Nitride; SiO: Silicon Oxide; *: CMOS Sensors; NR: Not Reported by the Author(s).

Table 2. MEMS Thermal Flow Sensors Fabricated on Polymer Substrates.

First Author, Year	[Ref]	Type	Sensor Material	Sensor Size ($l \times w \times t$, all in μm)	Substrate Material
Miau, 2006	[97]	Hot-Film	Platinum	$260 \times 200 \times 0.1$	Polyimide
Liu, 2007	[98]	Hot-Film	Platinum	$2100 \times 1500 \times 500$	Polyimide
Tan, 2007	[100]	Hot-Film	Gold//Chromium	$4000 \times 90 \times 0.3$	Polyimide
Buchner, 2008	[52]	Calorimetric	Titanium-Tungsten	$\text{NR} \times \text{NR} \times \text{NR}$	Polyimide
Liu, 2009	[106]	Hot-Film	Chromium/Nickel/Platinum	$3000 \times 300 \times 0.23$	Polyimide
Que, 2012	[111]	Hot-Film	Cr/Ni/Pt	$\text{NR} \times \text{NR} \times \text{NR}$	Polyimide
Li, 2015	[11]	Hot-Film	Gold	$\text{NR} \times \text{NR} \times \text{NR}$	Polyimide
Tang, 2016	[58]	Hot-Film	Platinum	$\text{NR} \times 5 \times 0.2$	Polyimide
Yu, 2016	[115]	Hot-Film	Chromium/Platinum	$200 \times 260 \times 0.12$	Polyimide
Yu, 2007	[101]	Hot-Film	Titanium/Platinum	$160 \times 80 \times 0.1$	Parylene C
Yu, 2008	[117]	Hot-Film	Titanium/Platinum	$280 \times 2 \times 0.075$	Parylene C
Chang, 2008	[103]	Hot-Film	Platinum	$\text{NR} \times \text{NR} \times \text{NR}$	Parylene C
Kuo, 2011	[110]	Hot-Film	Platinum	$\text{NR} \times \text{NR} \times \text{NR}$	Parylene C
Hasegawa, 2016	[114]	Hot-Film	Gold/Copper	$\text{NR} \times \text{NR} \times 0.26$	Parylene (Exact type NR)
Li, 2008	[104]	Hot-Film	Gold	$\text{NR} \times \text{NR} \times 0.1$	Kapton
Li, 2011	[9]	Hot-Film	Gold	$\text{NR} \times \text{NR} \times 0.12$	Kapton
Li, 2012	[10]	Hot-Film	Gold	$\text{NR} \times \text{NR} \times 0.12$	Kapton
Kaltsas, 2007	[50]	Hot-Film + Calorimetric	Platinum	$\text{NR} \times \text{NR} \times 0.3$	SU-8
Vilares, 2010	[54]	Calorimetric	Titanium/Platinum	$2500 \times 10 \times 0.15$	PMMA
Berthet, 2011	[72]	TOF	Titanium/Platinum	$500 \times 20 \times 20$	Pyrex

The ceramic materials with low thermal conductivity (k), used as substrate in MEMS thermal flow sensors and summarized in Table 1, include glass ($k = 1.1 \text{ W/(m}\cdot\text{K)}$ [57]), porous silicon

($k = 1.2 \text{ W}/(\text{m}\cdot\text{K})$ [45]), silicon nitride ($k = 20 \text{ W}/(\text{m}\cdot\text{K})$ [118]), aluminum oxide ($k = 20 \text{ W}/(\text{m}\cdot\text{K})$ [49]), as-grown polysilicon ($k = 13.8 \text{ W}/(\text{m}\cdot\text{K})$) and amorphous recrystallized polysilicon ($k = 22 \text{ W}/(\text{m}\cdot\text{K})$ [119]). Silicon, which has relatively higher thermal conductivity ($k = 130 \text{ W}/(\text{m}\cdot\text{K})$ [51]) has also been used as a substrate material in few cases. However, such substrates have generally been used in wind sensing applications, where sensors are mostly wafer thick [15].

Thermal conductivity of polymers is typically lower than the ceramics and these are also good candidate substrate materials, as summarized in Table 2, for reduced conduction losses in MEMS thermal flow sensors. Polyimide, with a thermal conductivity of $k = 0.29 \text{ W}/(\text{m}\cdot\text{K})$, has been most widely used as a substrate material [11,52,58,96–98,100,106,111,115]. Other substrate materials from polymers family include SU-8 ($k = 0.2 \text{ W}/(\text{m}\cdot\text{K})$ [50]), PMMA ($k = 0.1920\text{--}0.2 \text{ W}/(\text{m}\cdot\text{K})$), pyrex ($k = 1.3\text{--}1.5 \text{ W}/(\text{m}\cdot\text{K})$ [120]), Kapton ($k = 0.12 \text{ W}/(\text{m}\cdot\text{K})$ [121]), parylene N ($k = 0.13 \text{ W}/(\text{m}\cdot\text{K})$ [84]) and parylene C ($k = 0.082 \text{ W}/(\text{m}\cdot\text{K})$ [122]). Although, parylene N has higher thermal conductivity than parylene C, yet due to its higher melting temperature ($420 \text{ }^\circ\text{C}$), it is preferred as membrane material for the hot-film sensors over parylene C, which has a melting temperature of $290 \text{ }^\circ\text{C}$ [74].

Similarly, a review of the membrane-mounted MEMS thermal flow sensors illustrates that the membranes used for thermal isolation of the sensing heater (hot-element) are made of diverse materials and have different shapes and sizes. Most of these membranes are made of ceramics, with a handful made of polymer materials. For a quick reference, the MEMS thermal flow sensors having membranes of square, circular and rectangular shapes are grouped and their key information is summarized in Tables 3–5, respectively.

Table 3. MEMS Thermal Flow Sensors with Square Membranes.

First Author, Year	[Ref]	Type	Sensor Material	Sensor Size ($l \times w \times t$, all in μm)	Membrane Material	Membrane Size ($l \times w \times t$, all in μm)	MHR
Liu, 1994	[63]	Hot-Film	Polysilicon	$100 \times 2 \times 0.45$	SiN	$200 \times 200 \times 1.2$	2
Jiang, 1996	[65]	Hot-Film	Polysilicon	$150 \times 3 \times 0.25$	SiN	$200 \times 200 \times 1.2$	1.33
Huang, 1996	[64]	Hot-Film	Polysilicon	$80 \times 2 \times \text{NR}$	SiN	$200 \times 200 \times 1.2$	2.5
Jiang, 1997	[67]	Hot-Film	Polysilicon	$150 \times 3 \times 0.25$	SiN	$200 \times 200 \times 1.2$	1.33
Huang, 1999	[68]	Hot-Film	Polysilicon	$(100,150,200) \times (2,3,4) \times 1$	SiN	$200 \times 200 \times 2$	2
Liu, 1999	[69]	Hot-Film	Polysilicon	$100 \times 2 \times 0.45$	SiN	$200 \times 200 \times 1.5$	2
Hung, 2000	[70]	Hot-Film	Platinum	$\text{NR} \times \text{NR} \times 0.18$	SiN	$600 \times 600 \times 0.2$	-
Maily, 2001	[71]	Hot-Film	Platinum	$\text{NR} \times \text{NR} \times 0.3$	SiN	$650 \times 650 \times 0.5$	-
Yoshino, 2001	[72]	Hot-Film	Platinum	$200 \times 23 \times 0.1$ $300 \times 32 \times 0.1$	SiN	$400 \times 400 \times 1.0$ $500 \times 500 \times 1.0$	2
Xu, 2002	[73]	Hot-Film	Polysilicon	$150 \times 2 \times 0.5$	SiN	$210 \times (45\text{--}210) \times 4.2$	1.4
Xu, 2004	[75]	Hot-Film	Polysilicon	$150 \times 2 \times 0.5$	SiN	$210 \times (75\text{--}210) \times 4.2$	1.4
Xu, 2005	[123]	Hot-Film	Polysilicon	$150 \times 7 \times 0.5$	SiN	$210 \times 210 \times 1.5$	1.4
Xu, 2005	[124]	Hot-Film	Polysilicon	$180\text{--}210 \times \text{NR} \times 0.5$	SiN	$210 \times 45\text{--}210 \times 4.2$	1 – 1.16
Soundrarajan, 2005	[76]	Hot-Film	Polysilicon	$80 \times 2 \times 3$	SiN	$\text{NR} \times \text{NR} \times 0.3$	-
Kim, 2006	[77]	Hot-Film	Gold	$600 \times 50 \times 0.45$	SiN	$1000 \times 1000 \times 1.3$	1.66
Liang, 2008	[78]	Hot-Film	Titanium/Platinum	$100 \times 2 \times 0.2$	SiN	$200 \times 200 \times 1.5$	2
Sabate, 2004	[25]	Calorimetric	Nickel	$\text{NR} \times 40 \times 0.15$	SiN	$750 \times 750 \times 0.3$	-
Buchner, 2006	[26]	Calorimetric	Polysilicon	$\text{NR} \times \text{NR} \times 0.3$	SiN	$1000 \times 1000 \times \text{NR}$	-
Adamec, 2010	[39]	Calorimetric	Nickel	$\text{NR} \times \text{NR} \times \text{NR}$	SiN	$\text{NR} \times \text{NR} \times \text{NR}$	-
Sosna, 2010	[48]	TOF	NR	$1000 \times 10 \times 0.3$	SiN	$1000 \times 1000 \times 0.6,0.3$ $600 \times 800 \times 0.6$	1
Sosna, 2011	[50]	TOF	NR	$1000 \times 10 \times 0.3$	SiN	$1000 \times 1000 \times 0.6,0.3$	1
Laconte, 2004	[24]	Calorimetric	Polysilicon	$240 \times 240 \times 0.34$ (Active area)	SiN/SiO	$440 \times 440 \times 1$ $640 \times 640 \times 1$ $840 \times 840 \times 1$	1.83
Yu, 2008	[27]	Calorimetric	Platinum	$\text{NR} \times \text{NR} \times \text{NR}$	SiN/SiO	$1800 \times 1800 \times \text{NR}$	-
Cubckcu, 2010	[3]	Calorimetric	Germanium	$\text{NR} \times \text{NR} \times \text{NR}$	SiN/SiO	$1000 \times 1000 \times 1.4$	-
Hsiai, 2004	[8]	Hot-Film	Polysilicon	$80 \times 2 \times 0.5$	SiN/SiO	$100 \times 100 \times 1.5$	1.25
*Piotto, 2012	[28]	Calorimetric	Polysilicon	$\text{NR} \times \text{NR} \times \text{NR}$	SiO	$\text{NR} \times \text{NR} \times \text{NR}$	-
*Haneef, 2007	[125]	Hot-Film	Aluminum	$130 \times 3 \times 0.72$	SiO	$500 \times 500 \times \text{NR}$	3.84
*Haneef, 2008	[126]	Hot-Film	Aluminum	$130 \times 3 \times 0.72$ $18.5 \times 1.1 \times 0.72$	SiO	$500 \times 500 \times \text{NR}$ $266 \times 266 \times \text{NR}$	3.8414.3
Kalvesten, 1996	[66]	Hot-Film	Polysilicon	$300 \times 60 \times 30$	Polysilicon	$1500 \times 1500 \times 30$	5
*Xu, 2003	[74]	Hot-Film	Polysilicon	$200 \times \text{NR} \times 0.32$	Parylene N	$250 \times 100 \times 1.5$	1.25

Table 4. MEMS Thermal Flow Sensors with Circular Membranes.

First Author, Year	[Ref]	Type	Sensor Material	Sensor Size ($l \times w \times t$, all in μm)	Membrane Material	Membrane Size ($\text{Dia} \times t$, all in μm)	MHR
Breuer, 1999, 2000	[79, 80]	Hot-Film	Platinum	100 × 5 × 0.1	SiN	[210 × 0.15]	2.1
Qu, 2016	[22]	Hot-Film	Platinum	140 × NR × NR	SiN	NR × NR × 1.5	-
Cain, 2000	[81]	Hot-Film	Platinum	200 × 4 × 0.15	SiN	[200 × 0.15]	1
Cubckcu, 2010	[3]	Calorimetric	Germanium	NR × NR × NR	SiN/SiO	[1000 × 1.4]	-
Reyes-Romero, 2013	[30]	Calorimetric	Chromium	NR × NR × NR	SiN/SiO	[1000 × 1.4]	-
Reyes-Romero, 2013	[31]	Calorimetric	Chromium	NR × NR × NR	SiN/SiO	[1000 × 1.4]	-
*Haneef, 2014	[83]	Hot Film	Tungsten	200 × 2 × 0.3	SiO (with SiN passivation)	[250 × NR]	1.25
*De Luca, 2013	[5]	Calorimetric+ Hot-Film	Tungsten	400 × 2 × NR	SiO	[1200 × NR]	3
*De Luca, 2015	[6]	Calorimetric	Tungsten	400 × 2 × NR	SiO	[1200 × NR]	3
Fan, 2004	[82]	Hot-Film	Gold	[NR × 0.2]	Parylene C	[400 × 12]	-

Table 5. MEMS Thermal Flow Sensors with Rectangular Membranes.

First Author, Year	[Ref]	Type	Sensor Material	Sensor Size ($l \times w \times t$, All in μm)	Membrane Material	Membrane Size ($l \times w \times t$, all in μm)	MHR
Yoshino, 2003	[85]	Hot-Film	Platinum	250 × 30 × 0.1	SiN	350 × 200 × 1.0	1.4
Ma, 2009	[89]	Hot-Film	Platinum	4400 ID × 300 × 0.1	SiN	NR × NR × 1	-
Saremi, 2014	[91]	Hot-Film	Platinum	2700 × 13 × 0.3	SiN	3000 × 1000 × 450	1.11
Shi, 2006	[86]	Hot-Film	Polysilicon	200 × 4 × 0.45	SiN	250 × 200 × 1.5	1.25
Ernst, 2002	[127]	Calorimetric	Germanium	574 × 6 × 0.2	SiN	900 × 700 × 1.4	1.56
Hedrich, 2010	[33]	Calorimetric	Polysilicon	NR × NR × 0.3	SiN	300 × 600 × 0.15	-
Dalola, 2012	[34]	Hot-Film and Calorimetric	Germanium	600 × 35 × 0.26	SiN/SiO	1000 × 500 × 1.6	1.66
Talic, 2015	[42]	Calorimetric +Hot-Film	Chromium	NR × NR × 0.13	SiN/SiO	1000 × 500 × 1.57	-
Bruschi, 2005	[32]	Calorimetric	Polysilicon	NR × NR × NR	SiO	45 × 60 × NR	-
Liu, 2013	[13]	Hot-Film	Titanium/Platinum	NR × NR × 0.11	SiO	NR × NR × NR	-
*Wang, 1999	[84]	Hot-Film	Polysilicon	NR × NR × 0.32	Parylene N	NR × NR × 3.5 NR × NR × 0.7	-
Wu, 2016	[23]	Hot-Film	Platinum	NR × 10 × 0.5	Parylene C	NR × NR × NR	-
Shibata, 2014	[92]	Hot-Film	Gold/copper	NR × NR × 0.26	Polyimide	NR × NR × 5	-
Imaeda, 2015	[93]	Hot-Film	Gold/Copper	NR × NR × 0.26	Polyimide	1600 × 1700 × 5	-
Hepp, 2011	[40]	Calorimetric	Platinum	NR × NR × NR	Polyimide	NR × NR × 6	-
Strum, 2013	[41]	Calorimetric	Tungsten-Titanium	NR × NR × NR	Polyimide	200 - 600 × 800 × 9.6	-
Meng, 2008	[36]	TOF Calorimetric Hot-Film	Platinum	200 × 25 × 0.1	Parylene C	NR × NR × 6	-
Sturm, 2010	[38]	Calorimetric	Titanium/Tungsten	NR × NR × NR	SiN/Polyimide	NR × NR × NR	-
Etxebarria, 2016	[44]	Calorimetric	Nickel	NR × NR × 0.1	Polymer (Exact name NR)	NR × NR × NR	-
Nguyen, 1997	[35]	Calorimetric	Polysilicon	NR × NR × NR	Silicon	NR × NR × NR	-

A quick look at Tables 3–5 reveals that among ceramics, silicon nitride is the most widely used membrane material for thermal isolation of MEMS thermal flow sensors [22,25,26,33,39,59,60,63–65,67–73,75–81,85,86,89,127]. To further reduce the heat conduction, bi-layer membranes of silicon nitride and silicon oxides have also been reported [3,8,24,30,31,34,42,83,117]. Thermal conductivity of this bi-layer system depends upon the individual thickness of silicon nitride and silicon oxide layers. However, a typical thermal conductivity value for this bi-layer system is $k = 1.98 \text{ W/(m}\cdot\text{K)}$ [3].

Because of much lower thermal conductivity values, polyimide [40,41,92,94], parylene C [23,82] and parylene N [74,84] are the three commonly used membrane materials in thermal flow sensors from the polymers family.

Like other devices with membranes [128,129], besides choice of suitable materials, membrane shape and membrane [side length (for square membrane) or diameter (for circular membrane)] to heater (hot-film (length) ratio (*MHR*) are two other design variables that are required to be optimized in thermal flow sensors employing membranes for minimization of conduction heat losses from the heater (hot-film) to the substrate.

As mentioned earlier, membranes of three shapes (i.e., square, circular and rectangular) with different sizes (Tables 3–5) have been used in different MEMS thermal flow sensors reported in the literature. An analysis of these membranes-based hot-film thermal flow sensors reveals that the *MHR* of these sensors fall in the range of 1.0–14.3 (Table 3—square membranes), 1.0–3.0 (Table 4—circular membranes) and 1.25–1.66 (Table 5—rectangular membranes), respectively. Interestingly, it is only tacitly assumed in all the reports listed in these three tables that the conductive heat losses depend largely on *MHR*, since none of the studies published during the last two decades (Tables 3–5) has explored the effect of *MHR* on the thermal efficiency (thermal resistance) of the sensors and the conductive heat losses from the sensor (hot-film/heater) to the substrate through formal experiments.

In this paper, therefore, a systematic experimental investigations of the effects of *MHR* and membrane shape (square versus circular) on the thermal resistance (or conductive heat losses) of MEMS thermal [thin (hot) film] flow sensors are reported for the first time.

The scope of the paper is limited to minimize the conductive heat losses to the substrate, thereby achieving improved thermal performance of the hot-film flow sensors. The heat losses due to radiation and natural or forced convection have not been taken into account in this study.

The experimental investigation is carried on MEMS thermal (hot-film) flow sensors having silicon oxide membranes (with a very thin silicon nitride passivation layer on the top to protect the sensors and power tracks), fabricated through a 1 μm Silicon-on-Insulator (SOI) Complementary Metal Oxide Semiconductor (CMOS) process. It is pertinent to highlight that silicon oxide has very low thermal conductivity ($k = 1.4\text{W}/(\text{m}\cdot\text{K})$ [118]) and there are hardly any studies, excluding a few reported by our group [5,6,83,125,126,130,131], that utilize silicon oxide membranes for thermal isolation of MEMS thermal hot-film flow sensors produced through a commercial SOI CMOS process.

Eight such sensors, with two different membrane shapes (i.e., square and circular) and four Membranes to Heater length Ratios (i.e., $MHR = 1, 2, 3$ and 4) are fabricated and characterized. The membrane shape that achieves minimum conduction losses has been identified experimentally. The optimum membrane to heater ratios (*MHR*) for both square and circular membranes, beyond which further gain in thermal resistance of the sensor versus corresponding increase in sensor (membrane) size and related cost per sensor becomes un-economical, is also investigated.

The remaining paper is organized as follows: the design of SOI CMOS MEMS hot film sensor chips is presented in Section 2, followed by their fabrication in Section 3. Experimental results are discussed in Section 4. Finally, the conclusions are given in Section 5.

2. SOI CMOS MEMS Hot-Film Sensors Chip Design

MEMS hot-film sensors were designed using Cadence™ Virtuoso® layout editor. Figure 1 [131] is the Cadence layout of designed SOI CMOS MEMS multi sensor chip showing the layout of all eight sensors on the die. Eight flow sensors (i.e., FS1 to FS8), four with square and four with circular membranes, with each type having a *MHR* of 1, 2, 3 and 4, were designed. The dimensions (length \times width \times thickness) of the hot-film (i.e., $80\ \mu\text{m} \times 2\ \mu\text{m} \times 0.3\ \mu\text{m}$) were kept identical for all eight sensors. The square membranes' side lengths and circular membranes' diameters were maintained as $80\ \mu\text{m}$, $160\ \mu\text{m}$, $240\ \mu\text{m}$ and $320\ \mu\text{m}$ for achieving a $MHR = 1, 2, 3$ and 4 , respectively.

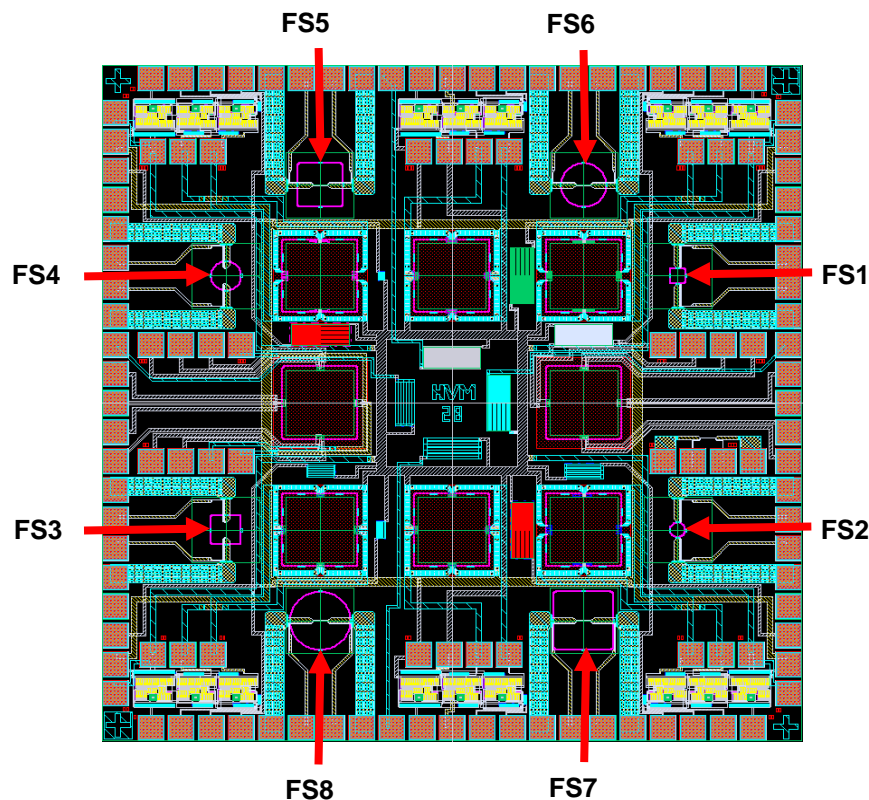


Figure 1. Cadence layout of the MEMS sensor chip which contains eight hot-film thermal flow sensors (FS1 to FS8) in it. The hot-film length is $80\ \mu\text{m}$ for all eight sensors. However, membrane side length/diameter for FS1 & FS2, FS3 & FS4, FS5 & FS6 and FS7 & FS8 is 80, 160, 240 and $320\ \mu\text{m}$, respectively. FS1, FS3, FS5 and FS7 (odd numbers) have square membranes, while FS2, FS4, FS6 and FS8 (even numbers) have circular membranes.

The details of the geometries of all eight SOI CMOS MEMS thermal hot-film flow sensors are given in Table 6. Tungsten, because of its superior mechanical (tensile strength, Young's modulus and density) and thermal properties (thermal conductivity and melting temperature) [6] is used as a hot-film and interconnects material. To achieve better thermal isolation and mechanical support for the hot-film, a $5.4\ \mu\text{m}$ thick silicon dioxide membrane is used to embed/support the tungsten hot-film sensors. A $0.55\ \mu\text{m}$ thick silicon nitride passivation layer is also deposited at the top of wafer to protect the metal tracks and sensors. The schematic cross-section of the tungsten hot-film designed thermal flow sensor is shown in Figure 2.

Table 6. Geometric Parameters of the Fabricated SOI CMOS MEMS Thermal Hot-Film Sensors.

Sensor Nomenclature	Membrane Shape	Membrane Size (Side Length/Diameter) μm	Heater (Hot-Film) Size ($l \times w \times t$) μm	Membrane to Heater Ratio (MHR)
FS1	Square	80	All heaters/hot-films have the same size ($80 \times 2 \times 0.3$)	1
FS2	Circular	80		2
FS3	Square	160		3
FS4	Circular	160		4
FS5	Square	240		
FS6	Circular	240		
FS7	Square	320		
FS8	Circular	320		

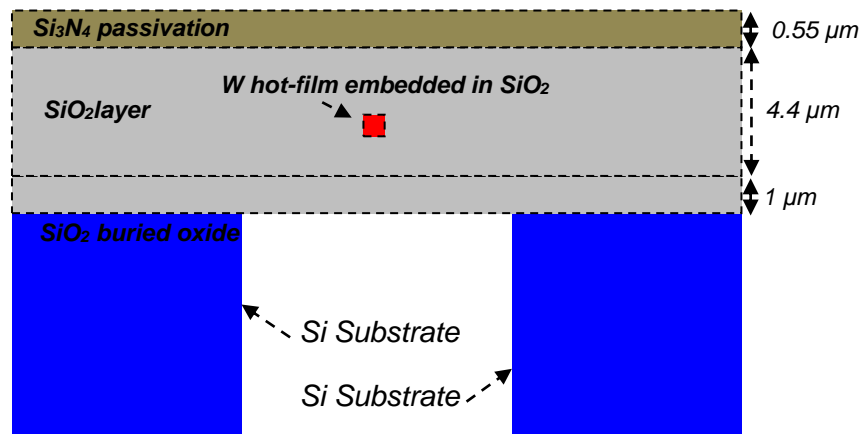


Figure 2. Schematic cross-section (not to the scale) of a tungsten hot-film thermal flow sensor.

3. SOI CMOS MEMS Hot-Film Sensors Chip Fabrication

Hot-film sensors are fabricated using 1- μm SOI CMOS process in a commercial CMOS MEMS foundry followed by a post-CMOS Deep Reactive Ion Etching (DRIE) process for creating cavities under membrane to further increase the thermal isolation of the hot-film sensors. A silicon substrate embedded with a buried oxide layer (i.e., SOI wafer) is used. The SOI technology provides four basic advantages; i.e., (a) the buried oxide acts as an etch stop layer for DRIE process, thus effectively controlling the etch depth and provides a uniform thickness to all sensor membranes, (b) provides a thermal isolation of sensing area, thus reducing the power losses to silicon substrate, (c) electrically isolates the electronic circuitry, reducing cross talk, and (d) increases the device operating temperatures range [132,133]. Cavities with vertical side walls are achieved using DRIE as it does not depend upon the lattice orientation of silicon substrate [6].

Optical micrographs of the fabricated sensors are shown in Figures 3 and 4. It is interesting to note from the optical micrographs of FS1 and FS2 sensors (Figure 3) that the cavities are not created underneath these sensors during the post-CMOS DRIE processing.

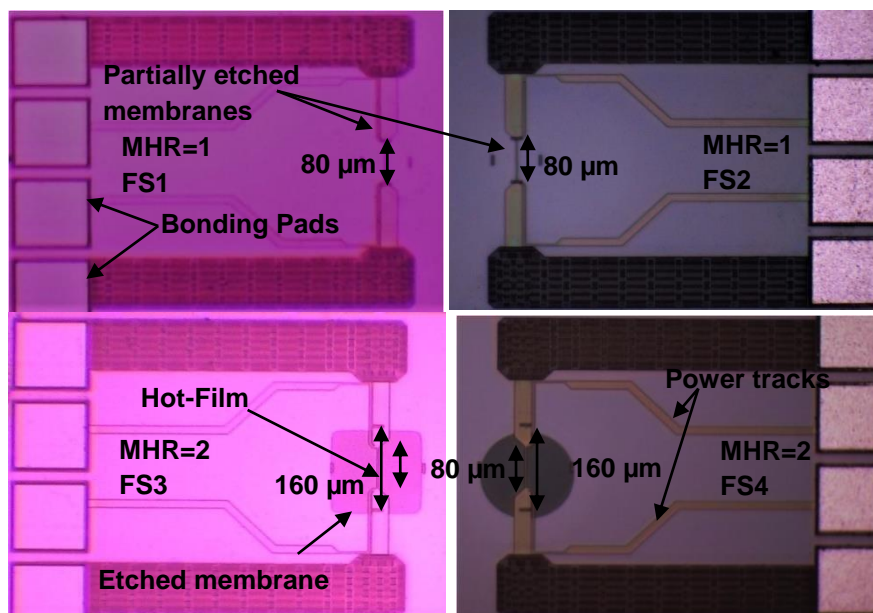


Figure 3. Optical micrographs (top view) of fabricated hot-film flow sensors having membrane to heater ratio $MHR = 1$ (FS1 and FS2) and $MHR = 2$ (FS3 and FS4).

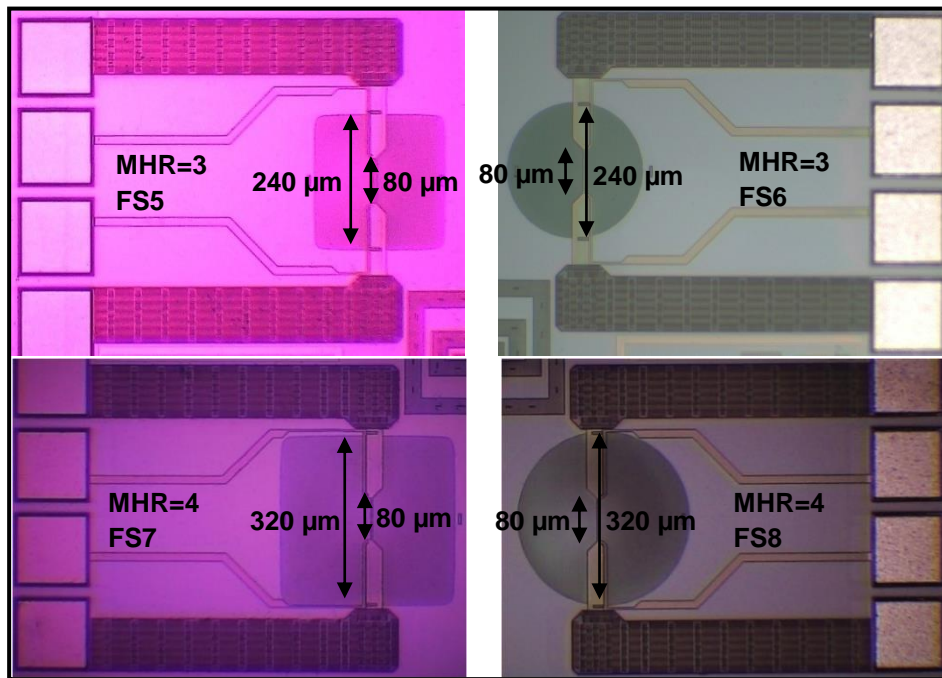


Figure 4. Optical micrographs (top view) of fabricated hot-film flow sensors having membrane to heater ratio $MHR = 3$ (FS5 and FS6).

The micro-sensors chip (Figure 1) containing FS1 and FS2 sensors has a variety of other (i.e., pressure and temperature) sensors as well with the membrane dimensions ranging from $80\ \mu\text{m}$ – $400\ \mu\text{m}$. Due to micro-loading effects and aspect ratio dependent etching [134,135], the membranes with the larger opening got etched earlier and the membranes (of smallest sensor, FS1 and FS2) with smaller opening (i.e., diameter = $80\ \mu\text{m}$) remained un-etched or partially etched. Therefore, these sensors are actually fabricated on the full substrate or only partially etched substrate, and will be discussed accordingly.

4. Experimental Results and Discussion

A Labview (National Instruments, Austin, TX, USA) data acquisition system integrated with a Keithley 2400 Source and Measuring Unit (SMU, Tektronix, Inc., Beaverton, OR, USA) and a Model S-1160 probe station (Signatone Corp, Gilroy, CA, USA) equipped with temperature controller and hot chuck are used for sensors' experimental (electro-thermal) characterization. In order to characterize the sensor for temperature coefficient of resistance (TCR), resistance variation of the tungsten heater from 25 – $150\ ^\circ\text{C}$ is obtained. Figure 5 is the plot of the temperature versus percentage change in resistance of the hot-film heater. The slope of this curve is the TCR of the tungsten hot-film sensors, which is approximately $0.22\%/^\circ\text{C}$. The TCR of the sensor is quite linear with a non-linearity of only 0.38% FS. A similar TCR value ($0.21\%/^\circ\text{C}$) has been reported earlier for tungsten thin film [83]. This TCR is almost double the value of polysilicon thin films (i.e., TCR of $0.13\%/^\circ\text{C}$) [69] and an order of magnitude higher than the carbon nano tubes (i.e., TCR of $0.04\ \%/^\circ\text{C}$) [99].

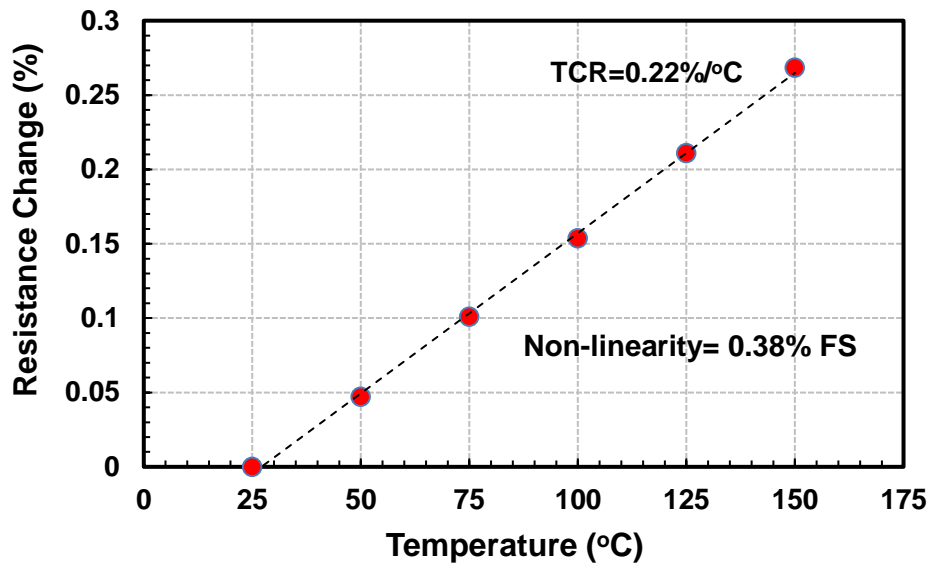


Figure 5. Temperature coefficient of resistance (TCR) of the tungsten based MEMS hot-film flow sensor.

Current-Voltage ($I - V$) and Power-Temperature ($P - T$) curves for all sensors are plotted to evaluate their electro-thermal characteristics. $I - V$ curves for the four hot-film sensors having square membrane (i.e., FS1, FS3, FS5 and FS7 with $MHR = 1, 2, 3$ and 4 , respectively) are shown in Figure 6 while their $P - T$ curves are depicted in Figure 7.

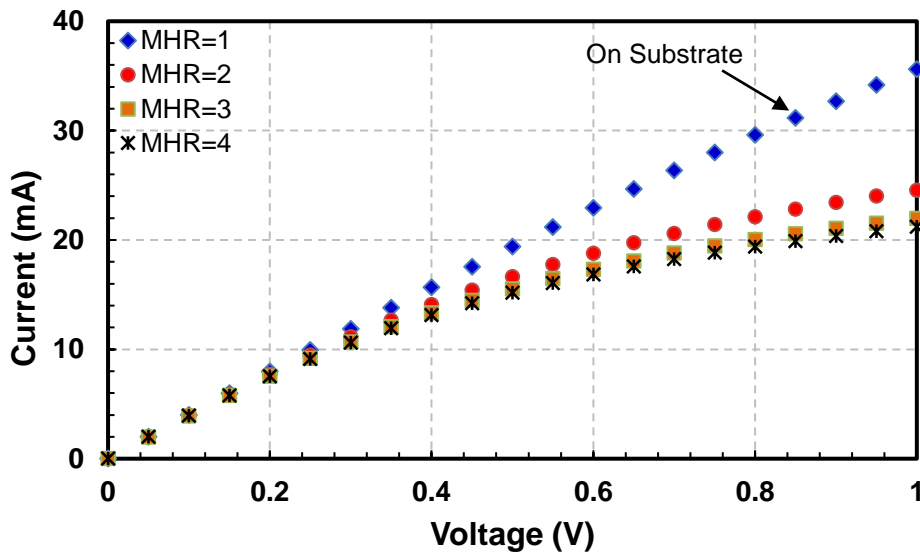


Figure 6. $I - V$ curves of SOI CMOS MEMS hot-film sensors FS1, FS3, FS5 and FS7 having square membranes: For FS1 sensor with $MHR = 1$ (that has partially etched membrane), the $I - V$ curve is almost linear indicating negligible change in sensor's resistance (i.e., no heating). With increasing MHR in FS3, FS5 and FS7 sensors (i.e., $MHR = 2, 3, 4$, respectively), the Joule heating and resistance increase significantly.

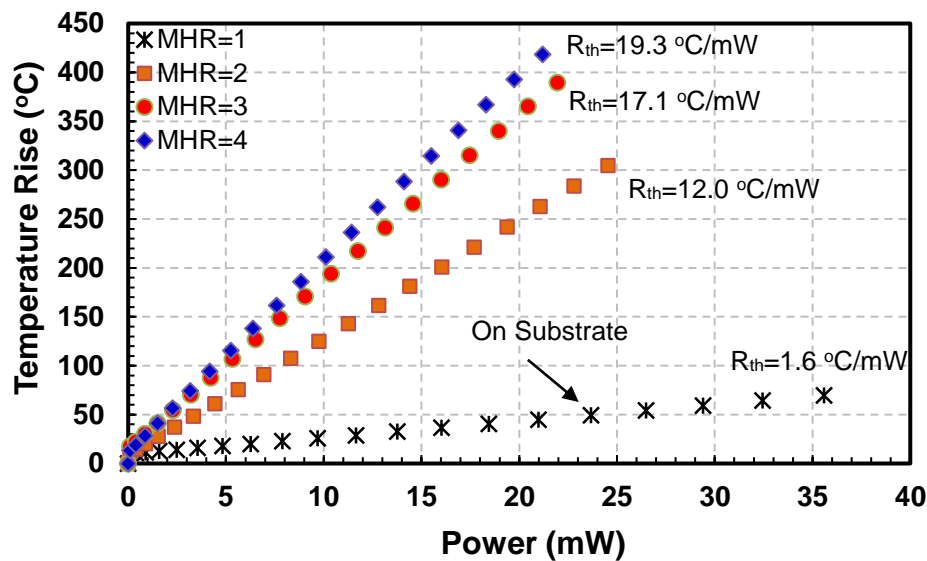


Figure 7. Power versus temperature rise curves for hot-film sensors FS1, FS3, FS5 and FS7 having square membranes: For FS1 sensor with $MHR = 1$ (having partially etched membrane), there is a negligible rise in sensor temperature. For FS3, FS5 and FS7 sensors with higher MHRs (i.e., $MHR = 2, 3, 4$, respectively), the temperature rise is significant, but its % increment between $MHR = 2$ to $MHR = 3$ and then from $MHR = 3$ to $MHR = 4$ reduces drastically.

The variations in $I - V$ curves are different with changing MHR . For $MHR = 1$ (FS1 sensor in Figure 3, which are actually fabricated on a partially etched substrate), current is almost directly proportional to the voltage (Figure 6). As expected, there is negligible joule heating and almost all the heat generated is being conducted straight into the substrate. The thermal resistance of the FS1 hot-film sensor is only $1.6 \text{ }^\circ\text{C/mW}$ (Figure 7). The effect of having a membrane under the sensor (i.e., thermal isolation of the hot-film sensor) is not visible in this plot as the membrane for FS1 was not created fully and only partial etching took place during the post-CMOSDRIE processing due to micro-loading effects and aspect ratio dependent etching [134,135].

The backside picture of the MEMS sensors chip is shown in Figure 8. The hot-films of the completely etched sensors can be seen from the rear side of the sensor chip. However, for sensor having $MHR = 1$, only a tiny bright dot can be seen, indicating a partial etching of the sensor. Thermal performance of un-etched thermal flow sensors has also been evaluated in the past. For example, Liang et al. [78] achieved a thermal resistance of $0.2 \text{ }^\circ\text{C/mW}$ for a titanium/platinum alloy strip of size $100 \text{ } \mu\text{m} \times 2 \text{ } \mu\text{m} \times 0.2 \text{ } \mu\text{m}$, directly fabricated on a silicon substrate. The thermal resistance in case of our FS1 sensor is comparatively higher, most likely, due to the fact that instead of silicon substrate a SOI substrate has been used, which has a very low thermal conductivity silicon oxide layer just underneath the hot-film. The other reason is that although all the silicon was not etched during the etching, still a partial etching did take place under the hot-film sensor (Figure 8), which reduced the amount of heat being lost to the substrate to some extent.

For FS3 sensor having square membrane with $MHR = 2$ (Figure 3), $I - V$ curve is nonlinear having decreasing slopes with increasing voltages (Figure 6). In this configuration, the amount of required current to the hot-film sensor is decreasing with the increasing voltage, which implies an increase in sensor's temperature due to joule heating. As shown in the $P - T$ curve (Figure 7), thermal resistance of the FS3 square membrane hot-film sensor with ($MHR = 2$) is $12 \text{ }^\circ\text{C/mW}$. FS3 sensor has an increment of $10.4 \text{ }^\circ\text{C/mW}$ in its thermal resistance compared to that of FS1 ($MHR = 1$, on partially etched substrate). This amounts to 650% increase in sensor's thermal efficiency and decrease in conduction losses for this sensor on square membrane. Similar trend can be observed in previously published reports as well.

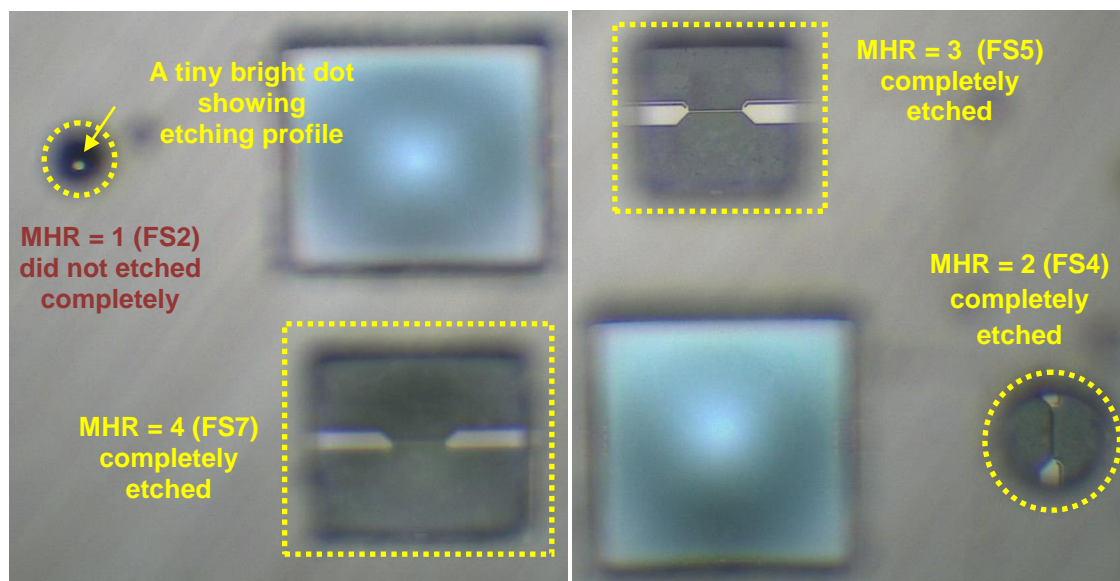


Figure 8. Optical micrograph of backside of the sensor chip, indicating the extent of etching for sensors with different *MHR*s. Hot-films are visible from the backside of the chip for *MHR*=2, 3 and 4, indicating a complete etching. For *MHR* = 1, a tiny bright dot can be seen, indicating only a partial etching.

For example, a polysilicon heater with dimensions $150\ \mu\text{m} \times 3\ \mu\text{m} \times 0.25\ \mu\text{m}$ and $MHR = 1.33$ had the sensitivity of $100\ \text{mV}/\text{Pa}$ [67], whereas another polysilicon silicon heater having dimensions $80\ \mu\text{m} \times 2\ \mu\text{m} \times 0.3\ \mu\text{m}$ and $MHR = 3.12$ has sensitivity of $1540\ \text{mV}/\text{Pa}$ [76], despite the fact that the hot-film length in the latter case was almost half that of the former. Similarly, in another study [78], the thermal resistance of a titanium/platinum heater on silicon nitride membrane having $MHR = 2$ was $6.8\ \text{°C}/\text{mW}$, whereas our tungsten hot-film sensor FS3 (with $MHR = 2$) on silicon oxide membrane achieved a thermal resistance $12\ \text{°C}/\text{mW}$, indicating a much better thermal isolation with silicon oxide membrane, which has lower thermal conductivity than silicon nitride. The reported thermal conductivity value of silicon oxide is $1.4\ \text{W}/(\text{m}\cdot\text{K})$, whereas that for silicon nitride is $20\ \text{W}/(\text{m}\cdot\text{K})$ [118], which in case of thin films may vary significantly depending upon the deposition parameters (e.g., thermal conductivity of a silicon nitride thin film is reported as $2.3\ \text{W}/(\text{m}\cdot\text{K})$ [91], while that for silicon oxide thin film it is documented as $1.1\ \text{W}/(\text{m}\cdot\text{K})$ [136]).

It is worth nothing, however, that thermal resistance (or conduction losses) of any hot-film flow sensor supported by a membrane depends upon both the membrane material (i.e., its thermal conductivity ' k ') and membrane geometry (i.e., membrane shape, its *MHR* and thickness ' t ').

For FS5 sensor with square membrane having $MHR = 3$ (Figure 4), the decrease in the slopes with increasing voltages of $I - V$ curve is more pronounced as compared with the FS3 sensor having $MHR = 2$ (Figure 6). The thermal resistance of the FS5 hot-film sensor is $17.1\ \text{°C}/\text{mW}$ (Figure 7). In comparison with the FS3 hot-films sensor having $MHR = 2$, an increase in thermal resistance of $5.1\ \text{°C}/\text{mW}$ has been achieved. This amounts to a further 42.5% increase in the sensor's thermal efficiency (or decrease in conduction losses).

For the FS7 hot-film sensor (Figure 4) with square membrane having $MHR = 4$, the decrease in the slopes with increasing voltages of $I - V$ curves is even more prominent as compared with FS1, FS3 and FS5 hot-film sensors (Figure 6). The thermal resistance of the FS7 hot-film sensor is $19.4\ \text{°C}/\text{mW}$ (Figure 7). The FS7 sensor with $MHR = 4$ has achieved an increment of $2.3\ \text{°C}/\text{mW}$ over the thermal resistance of FS5 sensor with $MHR = 3$. This amounts to 12.8% increase in sensor's thermal efficiency (or similar decrease in conduction losses).

It is worth noting that thermal resistance of the FS3 sensor (with $MHR = 2$) increased by 650% compared to that of the FS1 ($MHR = 1$, partially etched). This increment in thermal resistance for FS5 sensor ($MHR = 3$) compared to that of the FS3 sensor ($MHR = 2$) reduced to 42.5%. The improvement

in sensor's thermal efficiency (or thermal resistance) was further reduced to only 12.8% from FS5 sensor ($MHR = 3$) to the FS7 sensor ($MHR = 4$).

These experimental results thus point out that the gain in thermal efficiency (reduction in conduction losses or increase in thermal resistance) of the square membrane hot-film sensors for $MHR > 3$ is not much significant. However, at the same time, the increase in size of the sensor, which translates to increased price per sensor (as the price of CMOS sensor increases with the area occupied by it on CMOS processed wafer) and increase in sensor's fragility increases drastically.

To identify the exact membrane to heater ratio (MHR) beyond which gain in sensor's thermal efficiency is not economical in terms of excessively large chip area (or size), the percentage increase in square membrane sensors' membrane area versus the percentage increase in their thermal efficiency (or thermal resistance) is plotted in Figure 9. Both the percentage increase in MHR and sensor area have been calculated with respect to the sensor FS1 having $MHR = 1$.

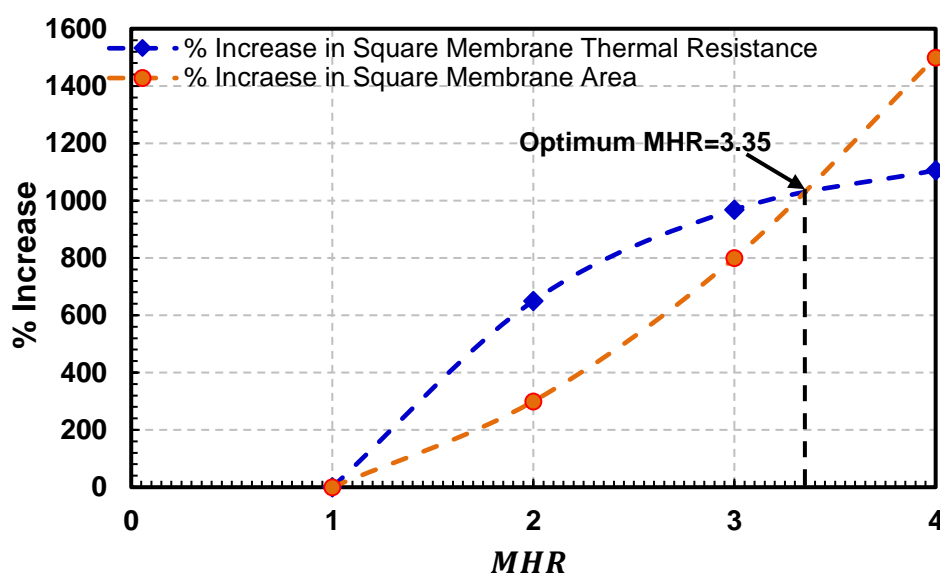


Figure 9. Plot showing the percentage increase in the square membrane area and the percentage increase in the thermal resistance with the increasing MHR for square membrane hot-film sensors FS1, FS3, FS5 and FS7. Up to $MHR = 3.35$, the percentage increase in sensors' thermal resistance is more pronounced viz-a-viz the percentage increase in the membrane area. However, beyond $MHR = 3.35$, the change is opposite, thus using a $MHR > 3.35$ for square membranes is not very economical in terms of corresponding sharp increase in sensor size.

It is evident from the figure that with increasing MHR , the percentage increase in the sensor's thermal resistance is more pronounced as compared with the percentage increase in sensor (membrane) area till MHR value of 3.35. However, an increase in sensor (membrane) area associated with MHR values greater than 3.35 is not matched with similar increase in the thermal resistance of the sensor. Thus, increasing sensor MHR beyond this value for a gain in its thermal resistance (or reduction in conductive losses) is not very economical viz-a-viz a corresponding sharp increase in membrane area or sensors size.

The effect of MHR on the thermal efficiency of hot-film sensors having circular membranes is similar to that of the hot-film sensors having square membranes. The $I - V$ curves for all four circular membrane hot-film sensors (i.e., FS2, FS4, FS6 and FS8 with $MHR = 1, 2, 3$ and 4, respectively) are shown in Figure 10 while $P - T$ curves are presented in Figure 11.

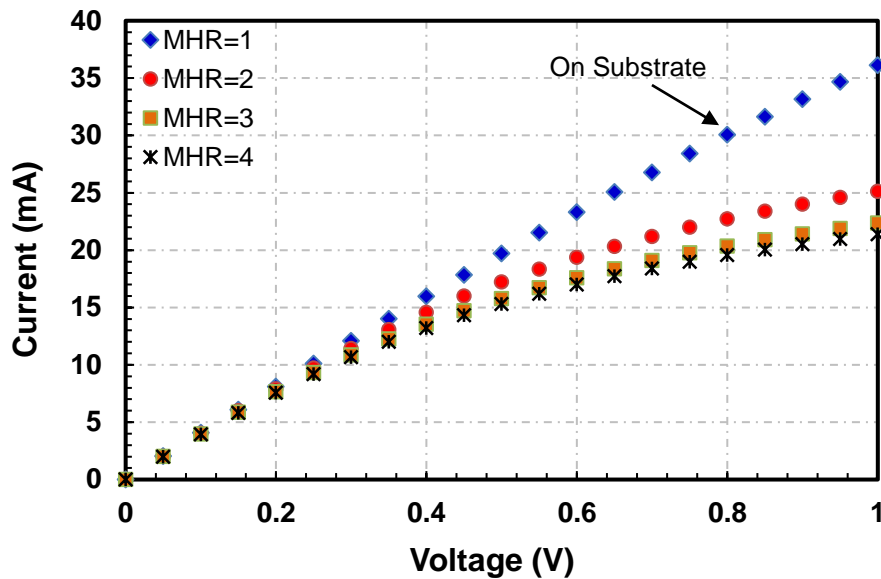


Figure 10. I – V curves of sensors FS2, FS4, FS6 and FS8 having circular membranes: For $MHR = 1$ (actually on substrate as membrane did not get etched), the I – V curve is almost linear indicating negligible change in sensor's resistance. With increasing MHR , however, sensors' Joule heating and resistances increase significantly.

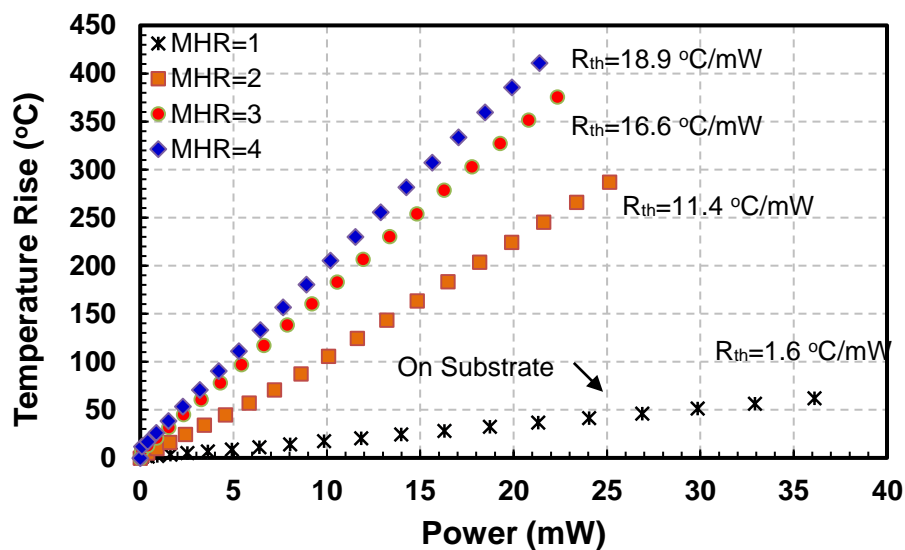


Figure 11. Power versus temperature rise curves of sensors FS2, FS4, FS6 and FS8 having circular membranes: For the FS2 sensor with $MHR = 1$ (on partially etched substrate), there is a negligible temperature rise in the sensor. There is a greater temperature rise between sensors with $MHR=2$ and 3, which reduces significantly for the sensor having $MHR = 4$.

For circular membrane hot-film sensor FS4 (Figure 3) having $MHR = 2$, the I – V curve is nonlinear, with decreasing slopes with increasing voltages (Figure 10), like the behavior exhibited by the square membrane hot-film sensor FS3 as well (Figure 6). The thermal resistance of the FS4 hot-film sensor is $11.4\text{ }^{\circ}\text{C}/\text{mW}$ (Figure 11). While comparing the temperature rise for this configuration with the former one (sensor on substrate), an increase of $9.8\text{ }^{\circ}\text{C}/\text{mW}$ in sensor's thermal resistance is recorded. This amounts to 512% increase in FS4 sensor's thermal efficiency (and decrease in conduction losses) over that of FS2 ($MHR = 1$) circular membrane sensor.

For circular membrane sensors having $MHR = 3, 4$ (FS6 and FS8 sensor in Figure 4), the decrease in the slopes with increasing voltages of I – V curve is more pronounced as compared with the sensor

having $MHR = 2$ (Figure 10). The thermal resistance of the circular membrane hot-film sensors FS6 and FS8 is $16.6\text{ }^{\circ}\text{C}/\text{mW}$ and $18.9\text{ }^{\circ}\text{C}/\text{mW}$, respectively (Figure 11). This amounts to 45.6% and 13.8% increase in thermal resistance of the circular membrane hot-film sensors from $MHR = 2$ to $MHR = 3$ and from $MHR = 3$ to $MHR = 4$, respectively.

A qualitatively similar trend has been observed in the previously reported thermal flow sensors as well. A tungsten heater with a circular membrane having $MHR = 1.25$ reported by Haneef et al. [83] had a sensitivity of $35\text{ mV}/\text{Pa}$, whereas a tungsten heater with a circular membrane having $MHR = 3$ reported by De Luca et al. [5] had a sensitivity of about $57.2\text{ mV}/\text{Pa}$. It is worth noting, however, that the later had three thermopiles covering a large membrane area that provided an additional heat loss route through silicon based thermopiles' to the membrane sides and substrate, due to which the hot-film sensor's sensitivity was not that pronounced in spite of having a more efficient MHR (i.e., 3.0) compared to that of the former case (i.e., 1.25 only).

Similar to the square membranes case, the exact membrane to heater ratio (MHR) for circular membranes beyond which gain in sensors thermal efficiency is not very economical has been identified by plotting the percentage increase in sensors area against the percentage increase in the sensor thermal resistance (Figure 12).

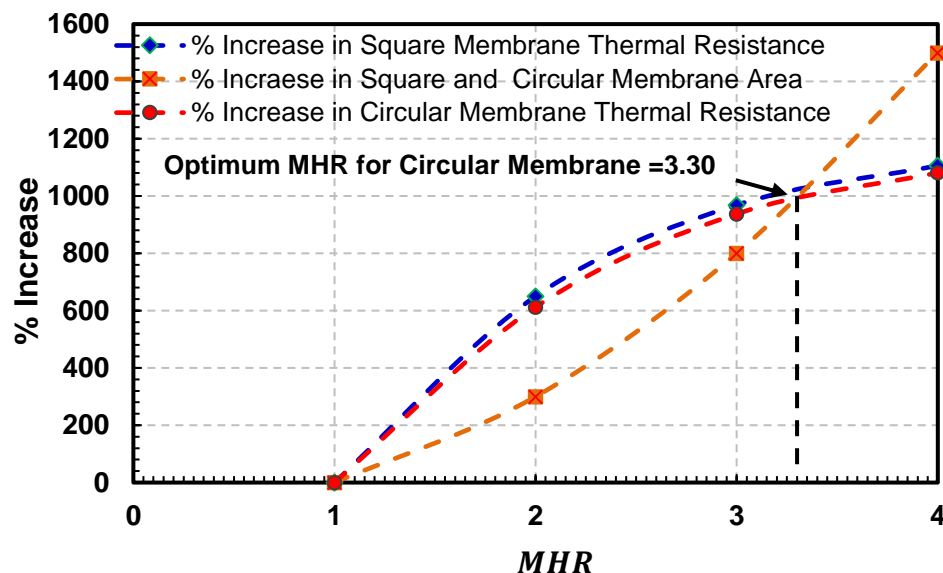


Figure 12. Plot showing the percentage increase in both square and circular membrane areas and increase in their thermal resistance with the increasing MHR . For circular membranes, the optimum $MHR = 3.30$, compared to the optimum $MHR = 3.35$ for square membranes.

It is evident from the figure that with increasing MHR , the percentage increase in the thermal resistance is more distinct in comparison with the percentage increase in the sensor (membrane) area till $MHR = 3.30$. However, this increase is insignificant beyond $MHR = 3.30$, in comparison with a corresponding sharp increase in sensor (membrane) area. Thus increasing MHR beyond 3.30 is not viable.

The effect of circular and square membrane shapes on thermal resistance (or conduction losses) of the hot-film sensors is given in Figure 13. In this figure, the sensors' MHR is plotted against sensors' thermal resistance (temperature rise per milli watts of supplied power) on left y-axis and % increase in the thermal efficiency of the square membrane as compared with that of the circular membrane on right y-axis. As shown in Figure 13, the thermal resistance of both type of membranes increases with increasing MHR . However, this increase is not very economical beyond a $MHR = 3.35$ for square membranes and $MHR = 3.30$ for circular membranes. The performance of the square membrane is relatively better than the circular membrane. The incremental difference between the thermal efficiency

of circular and square membrane hot-film sensors, however, decreases with an increase in MHR . Square membrane is 5.2% more efficient in terms of its thermal resistance than the circular membrane at $MHR = 2$, which reduces to 3.0% and 2.6% at $MHR = 3$ and $MHR = 4$, respectively.

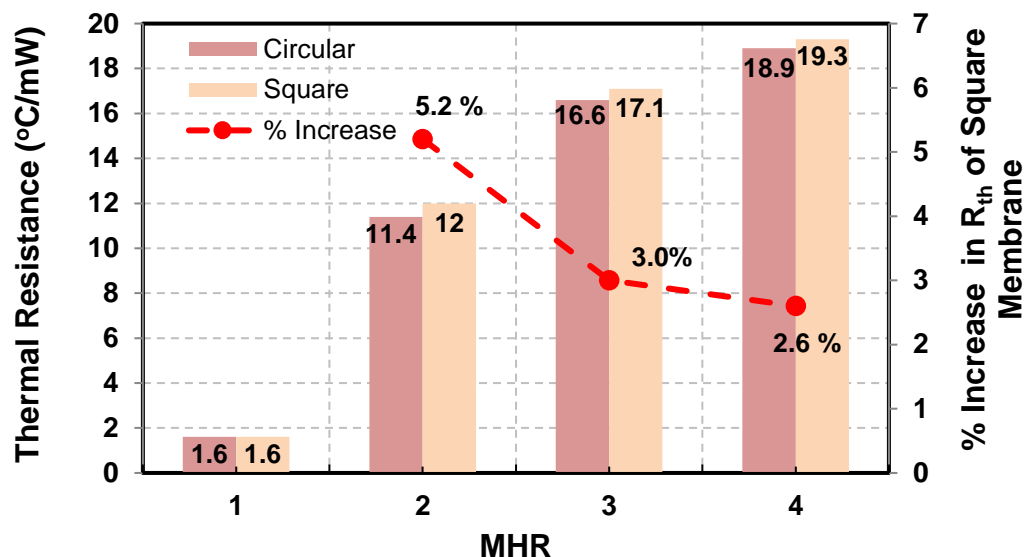


Figure 13. Thermal resistance (left y-axis) of square and circular membranes as a function of MHR compared on the bar graphs. Square membranes have relatively better thermal resistance. However with increasing MHR s, the % difference of thermal resistance between square and circular membranes (right y-axis) reduces significantly as shown by the line graph.

However, for higher membrane to heater ratios, it is more pragmatic to use circular membrane in hot-film flow sensors as it has a more uniform stress distribution at the edges with the substrate [6], thus achieving a better mechanical strength compared to that of the square membrane. It is pertinent to mention that for any specific mechanical loading, the maximum stresses generated on a square membrane are 64% higher than the circular membrane having the same material, thickness and diameter as of the side length of a square membrane [137].

5. Conclusions

Membrane heat conduction losses and their effects on SOI CMOS MEMS thermal (hot-film) flow sensor's thermal resistance as a function of membrane shape and Membrane to Heater (hot-film length) Ratio ($MHR = 1, 2, 3, 4$) have been investigated experimentally for the first time. For this purpose, electrical and thermal characterization of eight tungsten hot-film thermal flow sensors (four each having square and circular shapes) is carried out. The sensors were fabricated in a commercial 1 μm SOI CMOS foundry and then post-CMOS processed to create silicon oxide membranes under the hot-film sensors through a single DRIE back-etch step.

Experimental results demonstrate relatively lower conduction losses in square membranes-based hot-film MEMS flow sensors as compared with those having circular membranes. However, the conduction losses (or thermal resistance) difference between square and circular membranes decreases with increasing MHR . At $MHR = 2$, the circular membrane hot-film sensor had 5.2% lower thermal resistance than that of the square membrane hot-film sensor, which reduced to 3.0% and 2.6% for square and circular membrane sensors having $MHR = 3$ and $MHR = 4$, respectively. Since square membranes experience much higher mechanical stresses than circular membranes (stresses on square membranes are 1.64 times of that on circular membranes), therefore, in spite of slightly better thermal resistance of square membranes, circular membranes may be the optimal choice for MEMS thermal hot-film flow sensors for achieving higher mechanical strength and robustness.

The thermal resistance of both square and circular membrane hot film sensors increases with increase in MHR . However, beyond a $MHR = 3.35$ for square membranes and $MHR = 3.30$ for circular membranes, experimental results suggest that the gain in sensor's thermal resistance (reduction in conductive heat losses) is less significant as compared with the increase in the sensor (membrane) size, which adds to both the price and mechanical fragility of the sensor. It is therefore, neither cost effective nor mechanically preferable to have membrane to heater ratio (MHR) more than 3.35 and 3.30 for square and circular membranes-based SOI CMOS MEMS thermal hot-film flow sensors.

Author Contributions: Conceptualization, I.H. and S.Z.A.; methodology, Z.M.; validation, I.H., S.Z.A. and F.U.; formal analysis, Z.M.; investigation, Z.M.; resources, I.H. and F.U.; data curation, Z.M.; writing—original draft preparation, Z.M.; writing—review and editing, I.H., S.Z.A. and F.U.; supervision, I.H. and F.U.; project administration, I.H.; funding acquisition, I.H. and F.U.

Funding: This research was funded by British Council (BC) and Higher Education Commission (HEC), Pakistan grant No KEP-031 awarded to Ibraheem Haneef and Florin Udrea under BC-HEC Knowledge Economy Partnership (KEP) Programme.

Conflicts of Interest: On behalf of all the authors, I confirm that there is no actual or potential conflict of interest including any financial, personal or other relationships with other people or organizations.

References

- Janson, S.; Helvajian, H.; Breuer, K. MEMS, microengineering and aerospace systems. *AIAA Pap.* **1999**, *3802*. [[CrossRef](#)]
- Xu, Y.; Jiang, F.; Newbern, S.; Huang, A.; Ho, C.-M.; Tai, Y.-C. Flexible shear-stress sensor skin and its application to unmanned aerial vehicles. *Sens. Actuators A Phys.* **2003**, *105*, 321–329. [[CrossRef](#)]
- Cubukcu, A.S.; Zernickel, E.; Buerklin, U.; Urban, G.A. A 2D thermal flow sensor with sub-mW power consumption. *Sens. Actuators A Phys.* **2010**, *163*, 449–456. [[CrossRef](#)]
- Dominguez, M.; Jiménez, V.; Ricart, J.; Kowalski, L.; Torres, J.; Navarro, S.; Romeral, J.; Castañer, L. A hot film anemometer for the Martian atmosphere. *Planet. Space Sci.* **2008**, *56*, 1169–1179. [[CrossRef](#)]
- De Luca, A.; Haneef, I.; Coull, J.; Ali, S.; Falco, C.; Udrea, F. A thermopile based SOI CMOS MEMS wall shear stress sensor. In Proceedings of the IEEE International Semiconductor Conference (CAS 2013), Sinaia, Romania, 14–16 October 2013; pp. 59–62.
- De Luca, A.; Haneef, I.; Coull, J.D.; Ali, S.Z.; Falco, C.; Udrea, F. High-sensitivity single thermopile SOI CMOS MEMS thermal wall shear stress sensor. *IEEE Sens. J.* **2015**, *15*, 5561–5568. [[CrossRef](#)]
- Fleming, W.J. Overview of automotive sensors. *IEEE Sens. J.* **2001**, *1*, 296–308. [[CrossRef](#)]
- Hsiai, T.K.; Cho, S.K.; Wong, P.K.; Ing, M.H.; Salazar, A.; Hama, S.; Navab, M.; Demer, L.L.; Ho, C.-M. Micro sensors: Linking real-time oscillatory shear stress with vascular inflammatory responses. *Ann. Biomed. Eng.* **2004**, *32*, 189–201. [[CrossRef](#)]
- Li, C.; Wu, P.-M.; Hartings, J.A.; Wu, Z.; Ahn, C.H.; LeDoux, D.; Shutter, L.A.; Narayan, R.K. Smart catheter flow sensor for real-time continuous regional cerebral blood flow monitoring. *Appl. Phys. Lett.* **2011**, *99*, 233705. [[CrossRef](#)]
- Li, C.; Wu, P.-M.; Hartings, J.A.; Wu, Z.; Ahn, C.H.; Narayan, R.K. Cerebral blood flow sensor with in situ temperature and thermal conductivity compensation. In Proceedings of the 25th IEEE International Conference on Micro Electro Mechanical Systems (MEMS'12), Paris, France, 29 January–2 February 2012; pp. 1021–1024.
- Li, C.; Wu, P.-M.; Wu, Z.; Limnusun, K.; Mehan, N.; Mozayan, C.; Golanov, E.V.; Ahn, C.H.; Hartings, J.A.; Narayan, R.K. Highly accurate thermal flow microsensor for continuous and quantitative measurement of cerebral blood flow. *Biomed. Microdevices* **2015**, *17*, 1–7. [[CrossRef](#)] [[PubMed](#)]
- Kaanta, B.; Chen, H.; Lambertus, G.; Steinecker, W.; Zhdaneev, O.; Zhang, X. High sensitivity micro-thermal conductivity detector for gas chromatography. In Proceedings of the 22nd IEEE International Conference on Micro Electro Mechanical Systems (MEMS' 09), Sorrento, Italy, 25–29 January 2009; pp. 264–267.
- Liu, H.-B.; Lin, N.; Pan, S.-S.; Miao, J.; Norford, L.K. High sensitivity, miniature, full 2-D anemometer based on MEMS hot-film sensors. *IEEE Sens. J.* **2013**, *13*, 1914–1920. [[CrossRef](#)]
- Bruschi, P.; Dei, M.; Piotta, M. A low-power 2-D wind sensor based on integrated flow meters. *IEEE Sens. J.* **2009**, *9*, 1688–1696. [[CrossRef](#)]

15. Makinwa, K.; Huijsing, J. A wind sensor with an integrated low-offset instrumentation amplifier. In Proceedings of the 8th IEEE International Conference on Electronics, Circuits and Systems, Malta, 2–5 September 2001; pp. 1505–1508.
16. Makinwa, K.; Huijsing, J. A wind-sensor interface using thermal sigma delta modulation techniques. *Sens. Actuators A Phys.* **2001**, *92*, 280–285. [[CrossRef](#)]
17. Makinwa, K.A.; Huijsing, J.H. A smart wind sensor using thermal sigma-delta modulation techniques. *Sens. Actuators A Phys.* **2002**, *97*, 15–20. [[CrossRef](#)]
18. Hua, X.; Yun-feng, X.; Bing-he, M.; Si-yu, H.; Shi-zhao, Z.; Zhe-wei, C. Application of thermal shear stress gauge in study on shear stress measurement on underwater bed surface. *Procedia Eng.* **2015**, *116*, 663–669. [[CrossRef](#)]
19. Balakrishnan, V.; Phan, H.-P.; Dinh, T.; Dao, D.V.; Nguyen, N.-T. Thermal flow sensors for harsh environments. *Sensors* **2017**, *17*, 2061. [[CrossRef](#)] [[PubMed](#)]
20. Kuo, J.T.; Yu, L.; Meng, E. Micromachined thermal flow sensors—A review. *Micromachines* **2012**, *3*, 550–573. [[CrossRef](#)]
21. Wang, Y.-H.; Chen, C.-P.; Chang, C.-M.; Lin, C.-P.; Lin, C.-H.; Fu, L.-M.; Lee, C.-Y. MEMS-based gas flow sensors. *Microfluid. Nanofluid.* **2009**, *6*, 333–346. [[CrossRef](#)]
22. Ou, Y.; Qu, F.; Wang, G.; Nie, M.; Li, Z.; Ou, W.; Xie, C. A MEMS thermal shear stress sensor produced by a combination of substrate-free structures with anodic bonding technology. *Appl. Phys. Lett.* **2016**, *109*, 023512. [[CrossRef](#)]
23. Wu, C.-H.; Kang, D.; Chen, P.-H.; Tai, Y.-C. MEMS thermal flow sensors. *Sens. Actuators A Phys.* **2016**, *241*, 135–144. [[CrossRef](#)]
24. Laconte, J.; Dupont, C.; Flandre, D.; Raskin, J.-P. SOI CMOS compatible low-power microheater optimization for the fabrication of smart gas sensors. *IEEE Sens. J.* **2004**, *4*, 670–680. [[CrossRef](#)]
25. Sabaté, N.; Santander, J.; Fonseca, L.; Gràcia, I.; Cané, C. Multi-range silicon micromachined flow sensor. *Sens. Actuators A Phys.* **2004**, *110*, 282–288. [[CrossRef](#)]
26. Buchner, R.; Sosna, C.; Maiwald, M.; Benecke, W.; Lang, W. A high-temperature thermopile fabrication process for thermal flow sensors. *Sens. Actuators A Phys.* **2006**, *130*, 262–266. [[CrossRef](#)]
27. Yu, B.; Gan, Z.; Cao, S.; Xu, J.; Liu, S. A micro channel integrated gas flow sensor for high sensitivity. In Proceedings of the 11th IEEE Intersociety Conference on Thermal and Thermomechanical Phenomena in Electronic Systems (ITHERM' 08), Orlando, FL, USA, 28–31 May 2008; pp. 215–220.
28. Piotto, M.; Dei, M.; Butti, F.; Pennelli, G.; Bruschi, P. Smart flow sensor with on-chip CMOS interface performing offset and pressure effect compensation. *IEEE Sens. J.* **2012**, *12*, 3309–3317. [[CrossRef](#)]
29. Issa, S.; Lang, W. Minimum detectable air velocity by thermal flow sensors. *Sensors* **2013**, *13*, 10944–10953. [[CrossRef](#)] [[PubMed](#)]
30. Reyes-Romero, D.F.; Cubukcu, A.S.; Urban, G.A. Measurement and simulation of the frequency response of a thermal flow sensor at different flow speeds. *Sens. Actuators A Phys.* **2013**, *189*, 168–176. [[CrossRef](#)]
31. Romero, D.F.R.; Kogan, K.; Cubukcu, A.S.; Urban, G.A. Simultaneous flow and thermal conductivity measurement of gases utilizing a calorimetric flow sensor. *Sens. Actuators A Phys.* **2013**, *203*, 225–233. [[CrossRef](#)]
32. Bruschi, P.; Diligenti, A.; Navarrini, D.; Piotto, M. A double heater integrated gas flow sensor with thermal feedback. *Sens. Actuators A Phys.* **2005**, *123*, 210–215. [[CrossRef](#)]
33. Hedrich, F.; Kliche, K.; Storz, M.; Billat, S.; Ashauer, M.; Zengerle, R. Thermal flow sensors for MEMS spirometric devices. *Sens. Actuators A Phys.* **2010**, *162*, 373–378. [[CrossRef](#)]
34. Dalola, S.; Cerimovic, S.; Kohl, F.; Beigelbeck, R.; Schalko, J.; Ferrari, V.; Marioli, D.; Keplinger, F.; Sauter, T. MEMS thermal flow sensor with smart electronic interface circuit. *IEEE Sens. J.* **2012**, *12*, 3318–3328. [[CrossRef](#)]
35. Nguyen, N.; Dötzel, W. Asymmetrical locations of heaters and sensors relative to each other using heater arrays: A novel method for designing multi-range electrocaloric mass-flow sensors. *Sens. Actuators A Phys.* **1997**, *62*, 506–512. [[CrossRef](#)]
36. Meng, E.; Li, P.-Y.; Tai, Y.-C. A biocompatible Parylene thermal flow sensing array. *Sens. Actuators A Phys.* **2008**, *144*, 18–28. [[CrossRef](#)]
37. Bruschi, P.; Nurra, V.; Piotto, M. A compact package for integrated silicon thermal gas flow meters. *Microsyst. Technol.* **2008**, *14*, 943–949. [[CrossRef](#)]

38. Sturm, H.; Brauns, E.; Froehner, K.; Lang, W.; Buchner, R. Thermoelectric flow sensors on flexible substrates and their integration process. In Proceedings of the IEEE Conference on Sensors (SENSORS'10), Kona, HI, USA, 1–4 November 2010; pp. 575–579.
39. Adamec, R.J.; Thiel, D.V. Self heated thermo-resistive element hot wire anemometer. *IEEE Sens. J.* **2010**, *10*, 847–848. [[CrossRef](#)]
40. Hepp, C.; Krogmann, F.; Polak, J.; Lehmann, M.; Urban, G. AC characterisation of thermal flow sensor with fluid characterisation feature. In Proceedings of the 16th IEEE Conference on International Solid-State Sensors, Actuators and Microsystems, Beijing, China, 5–9 June 2011; pp. 1084–1087.
41. Sturm, H.; Lang, W. Membrane-based thermal flow sensors on flexible substrates. *Sens. Actuators A Phys.* **2013**, *195*, 113–122. [[CrossRef](#)]
42. Talic, A.; Cerimovic, S.; Beigelbeck, R.; Kohl, F.; Sauter, T.; Keplinger, F. MEMS flow sensors based on self-heated aGe-thermistors in a wheatstone bridge. *Sensors* **2015**, *15*, 10004–10025. [[CrossRef](#)]
43. Zhu, P.; Ma, B.; Jiang, C.; Deng, J.; Wang, Y. Improved sensitivity of micro thermal sensor for underwater wall shear stress measurement. *Microsyst. Technol.* **2015**, *21*, 785–789. [[CrossRef](#)]
44. Etxebarria, J.; Berganzo, J.; Elizalde, J.; Llamazares, G.; Fernández, L.J.; Ezkerra, A. Low cost polymeric on-chip flow sensor with nanoliter resolution. *Sens. Actuators B Chem.* **2016**, *235*, 188–196. [[CrossRef](#)]
45. Kaltsas, G.; Nassiopoulou, A. Novel CMOS-compatible monolithic silicon gas flow sensor with porous silicon thermal isolation. *Sens. Actuators A Phys.* **1999**, *76*, 133–138. [[CrossRef](#)]
46. Kaltsas, G.; Nassiopoulos, A.A.; Nassiopoulou, A.G. Characterization of a silicon thermal gas-flow sensor with porous silicon thermal isolation. *IEEE Sens. J.* **2002**, *2*, 463–475. [[CrossRef](#)]
47. Matova, S.P.; Makinwa, K.A.; Huijsing, J.H. Compensation of packaging asymmetry in a 2-D wind sensor. *IEEE Sens. J.* **2003**, *3*, 761–765. [[CrossRef](#)]
48. Fürjes, P.; Légrádi, G.; Dücső, C.; Aszódi, A.; Bársony, I. Thermal characterisation of a direction dependent flow sensor. *Sens. Actuators A Phys.* **2004**, *115*, 417–423. [[CrossRef](#)]
49. Sun, J.-B.; Qin, M.; Huang, Q.-A. Flip-chip packaging for a two-dimensional thermal flow sensor using a copper pillar bump technology. *IEEE Sens. J.* **2007**, *7*, 990–995. [[CrossRef](#)]
50. Kaltsas, G.; Petropoulos, A.; Tsougeni, K.; Pagonis, D.; Speliotis, T.; Gogolides, E.; Nassiopoulou, A. A novel microfabrication technology on organic substrates-application to a thermal flow sensor. *J. Phys. Conf. Ser.* **2007**, *92*, 012046. [[CrossRef](#)]
51. Dijkstra, M.; de Boer, M.; Berenschot, J.; Lammerink, T.; Wiegerink, R.; Elwenspoek, M. Miniaturized thermal flow sensor with planar-integrated sensor structures on semicircular surface channels. *Sens. Actuators A Phys.* **2008**, *143*, 1–6. [[CrossRef](#)]
52. Buchner, R.; Froehner, K.; Sosna, C.; Benecke, W.; Lang, W. Toward flexible thermoelectric flow sensors: A new technological approach. *J. Microelectromech. Syst.* **2008**, *17*, 1114–1119. [[CrossRef](#)]
53. Stamatopoulos, C.; Petropoulos, A.; Mathioulakis, D.; Kaltsas, G. Study of an integrated thermal sensor in different operational modes, under laminar, transitional and turbulent flow regimes. *Exp. Therm. Fluid Sci.* **2008**, *32*, 1687–1693. [[CrossRef](#)]
54. Vilares, R.; Hunter, C.; Ugarte, I.; Aranburu, I.; Berganzo, J.; Elizalde, J.; Fernandez, L. Fabrication and testing of a SU-8 thermal flow sensor. *Sens. Actuators B Chem.* **2010**, *147*, 411–417. [[CrossRef](#)]
55. Xiang, D.; Yang, Y.; Xu, Y.; Li, Y. MEMS-based shear-stress sensor for skin-friction measurements. In Proceedings of the IEEE Conference on Instrumentation and Measurement Technology, Austin, TX, USA, 3–6 May 2010; pp. 656–661.
56. Shen, G.-P.; Qin, M.; Huang, Q.-A.; Zhang, H.; Wu, J. A FCOB packaged thermal wind sensor with compensation. *Microsyst. Technol.* **2010**, *16*, 511–518. [[CrossRef](#)]
57. Zhu, Y.-Q.; Chen, B.; Qin, M.; Huang, J.-Q.; Huang, Q.-A. Development of a self-packaged 2D MEMS thermal wind sensor for low power applications. *J. Micromech. Microeng.* **2015**, *25*, 085011. [[CrossRef](#)]
58. Tang, J.; Zhang, W.; Liu, W.; Chen, H.; Sun, Y. Research on a micromachined flexible hot-wire sensor array for underwater wall shear stress measurement. *Microsyst. Technol.* **2016**, *23*, 2781–2788. [[CrossRef](#)]
59. Sosna, C.; Walter, T.; Lang, W. Response time of thermal flow sensors. *Procedia Eng.* **2010**, *5*, 524–527. [[CrossRef](#)]
60. Sosna, C.; Walter, T.; Lang, W. Response time of thermal flow sensors with air as fluid. *Sens. Actuators A Phys.* **2011**, *172*, 15–20. [[CrossRef](#)]

61. Van Kuijk, J.; Lammerink, T.; De Bree, H.-E.; Elwenspoek, M.; Fluitman, J. Multi-parameter detection in fluid flows. *Sens. Actuators A Phys.* **1995**, *47*, 369–372. [[CrossRef](#)]
62. Berthet, H.; Jundt, J.; Durivault, J.; Mercier, B.; Angelescu, D. Time-of-flight thermal flowrate sensor for lab-on-chip applications. *Lab Chip* **2011**, *11*, 215–223. [[CrossRef](#)] [[PubMed](#)]
63. Liu, C.; Tai, Y.-C.; Huang, J.-B.; Ho, C.-M. Surface micromachined thermal shear stress sensor. *Electr. Eng.* **1994**, *116*, 81.
64. Huang, J.-B.; Tung, S.; Ho, C.-M.; Liu, C.; Tai, Y.-C. Improved micro thermal shear-stress sensor. *IEEE Trans. Instrum. Meas.* **1996**, *45*, 570–574. [[CrossRef](#)]
65. Jiang, F.; Tai, Y.-C.; Gupta, B.; Goodman, R.; Tung, S.; Huang, J.-B.; Ho, C.-M. A surface-micromachined shear stress imager. In Proceedings of the 9th IEEE Annual International Workshop on Micro Electro Mechanical Systems, San Diego, CA, USA, 11–15 February 1996; pp. 110–115.
66. Kälvesten, E.; Vieider, C.; Löfdahl, L.; Stemme, G. An integrated pressure—flow sensor for correlation measurements in turbulent gas flows. *Sens. Actuators A Phys.* **1996**, *52*, 51–58. [[CrossRef](#)]
67. Jiang, F.; Tai, Y.-C.; Walsh, K.; Tsao, T.; Lee, G.-B.; Ho, C.-M. A flexible MEMS technology and its first application to shear stress sensor skin. In Proceedings of the Tenth IEEE Annual International Workshop on Micro Electro Mechanical Systems (MEMS'97), Nagoya, Japan, 26–30 January 1997; pp. 465–470.
68. Huang, J.; Jiang, F.; Tai, Y.; Ho, C. A micro-electro-mechanical-system-based thermal shear-stress sensor with self-frequency compensation. *Meas. Sci. Technol.* **1999**, *10*, 687. [[CrossRef](#)]
69. Liu, C.; Huang, J.-B.; Zhu, Z.; Jiang, F.; Tung, S.; Tai, Y.-C.; Ho, C.-M. A micromachined flow shear-stress sensor based on thermal transfer principles. *J. Microelectromech. Syst.* **1999**, *8*, 90–99.
70. Hung, S.-T.; Wong, S.-C.; Fang, W. The development and application of microthermal sensors with a mesh-membrane supporting structure. *Sens. Actuators A Phys.* **2000**, *84*, 70–75. [[CrossRef](#)]
71. Maily, F.; Giani, A.; Bonnot, R.; Temple-Boyer, P.; Pascal-Delannoy, F.; Foucaran, A.; Boyer, A. Anemometer with hot platinum thin film. *Sens. Actuators A Phys.* **2001**, *94*, 32–38. [[CrossRef](#)]
72. Yoshino, T.; Suzuki, Y.; Kasagi, N.; Kamiunten, S. Assessment of the wall shear stress measurement with arrayed micro hot-film sensors in a turbulent channel flow. In Proceedings of the Second International Symposium on Turbulence and Shear Flow Phenomena, Stockholm, Sweden, 27–29 June 2001; pp. 153–158.
73. Xu, Y.; Jiang, F.; Lin, Q.; Clendenen, J.; Tung, S.; Tai, Y.-C. Underwater shear-stress sensor. In Proceedings of the Fifteenth IEEE International Conference on Micro Electro Mechanical Systems (MEMS' 02), Las Vegas, NV, USA, 24–24 January 2002; pp. 340–343.
74. Xu, Y.; Tai, Y.-C.; Huang, A.; Ho, C.-M. IC-integrated flexible shear-stress sensor skin. *J. Microelectromech. Syst.* **2003**, *12*, 740–747.
75. Xu, Y.; Clendenen, J.; Tung, S.; Jiang, F.; Tai, Y.-C. Underwater flexible shear-stress sensor skins. In Proceedings of the 17th IEEE International Conference on Micro Electro Mechanical Systems (MEMS '04), Maastricht, The Netherlands, 25–29 January 2004; pp. 833–836.
76. Soundararajan, G.; Rouhanizadeh, M.; Yu, H.; DeMaio, L.; Kim, E.; Hsiai, T.K. MEMS shear stress sensors for microcirculation. *Sens. Actuators A Phys.* **2005**, *118*, 25–32. [[CrossRef](#)]
77. Kim, I.C.; Lee, S.J. Characterization of a miniature thermal shear-stress sensor with backside connections. *Sens. Actuators A Phys.* **2006**, *128*, 305–311. [[CrossRef](#)]
78. Liang, Y.; Yi, O.; Sha-Li, S.; Jin, M.; Da-Peng, C.; Tian-Chun, Y. Micro thermal shear stress sensor based on vacuum anodic bonding and bulk-micromachining. *Chin. Phys. B* **2008**, *17*, 2130. [[CrossRef](#)]
79. Breuer, K.S.; Bayt, R.L.; Nayaar, A. Measurement of shear stress and temperature using MEMS fabricated sensors. In *Proceedings of ASME MEMS*; ASME: New York, NY, USA, 1999.
80. Breuer, K. MEMS sensors for aerodynamic measurements—the good, the bad (and the ugly). In Proceedings of the 38th Aerospace Sciences Meeting and Exhibit, Reno, NV, USA, 10–13 January 2000; p. 251.
81. Cain, A.; Chandrasekaran, V.; Nishida, T.; Sheplak, M. Development of a wafer-bonded, silicon-nitride membrane thermal shear-stress sensor with platinum sensing element. In Proceedings of the Technical Digest, Solid-State Sensor and Actuator Workshop, Hilton Head, SC, USA, 8–11 June 2000; pp. 300–303.
82. Fan, Z.; Engel, J.M.; Chen, J.; Liu, C. Parylene surface-micromachined membranes for sensor applications. *J. Microelectromech. Syst.* **2004**, *13*, 484–490. [[CrossRef](#)]
83. Haneef, I.; Umer, M.; Mansoor, M.; Akhtar, S.; Rafiq, M.; Ali, S.; Udrea, F. A tungsten based SOI CMOS MEMS wall shear stress sensor. In Proceedings of the IEEE Conference on Sensors (SENSORS'14), Valencia, Spain, 2–5 November 2014; pp. 1475–1478.

84. Wang, X.-Q.; Han, Z.; Jiang, F.; Tsao, T.; Lin, Q.; Tai, Y.-C.; Koosh, V.; Goodman, R.; Lew, J.; Ho, C.-M. A fully integrated shear stress sensor. In Proceedings of the International Conference on Solid-State Sensors and Actuators (Transducer), Sandai, Japan, 7–10 June 1999; pp. 1074–1077.
85. Yoshino, T.; Suzuki, Y.; Kasagi, N.; Kamiunten, S. Optimum design of microthermal flow sensor and its evaluation in wall shear stress measurement. In Proceedings of the Sixteenth IEEE Annual International Conference on Micro Electro Mechanical Systems (MEMS'03), Kyoto, Japan, 23 January 2003; pp. 193–196.
86. Shi, S.; Chen, D.; Bai, H.; Ding, D.; Ou, Y.; Ye, T.; Shen, G. A novel micro thermal shear stress sensor with a cavity underneath. In Proceedings of the 1st IEEE International Conference on Nano/Micro Engineered and Molecular Systems, Zhuhai, China, 18–21 January 2006; pp. 466–469.
87. Potts, J.R.; Lunnon, I.; Crowther, W.J.; Johnson, G.A.; Hucker, M.J.; Warsop, C. Development of a transonic wind tunnel test bed for MEMS flow control actuators and sensors. In Proceedings of the 47th AIAA Aerospace Sciences Meeting, Orlando, FL, USA, 5–8 January 2009; p. 319.
88. Liang, J.-M.; Yang, D.-G.; Li, J.-Q.; Jiang, W.-M.; Li, C.-Y. Calibration of a thermal MEMS shear stress sensor array. In Proceedings of the IEEE Symposium on Piezoelectricity, Acoustic Waves and Device Applications (SPAWDA'12), Shanghai, China, 23–25 November 2012; pp. 433–437.
89. Ma, R.-H.; Wang, D.-A.; Hsueh, T.-H.; Lee, C.-Y. A MEMS-based flow rate and flow direction sensing platform with integrated temperature compensation scheme. *Sensors* **2009**, *9*, 5460–5476. [[CrossRef](#)] [[PubMed](#)]
90. Laghrouche, M.; Montes, L.; Boussey, J.; Meunier, D.; Ameer, S.; Adane, A. In situ calibration of wall shear stress sensor for micro fluidic application. *Procedia Eng.* **2011**, *25*, 1225–1228. [[CrossRef](#)]
91. Saremi, S.; Alyari, A.; Feili, D.; Seidel, H. A MEMS-based hot-film thermal anemometer with wide dynamic measurement range. In Proceedings of the IEEE Conference on Sensors (SENSORS'2014), Valencia, Spain, 2–5 November 2014; pp. 420–423.
92. Shibata, S.; Niimi, Y.; Shikida, M. Flexible thermal MEMS flow sensor based on Cu on polyimide substrate. In Proceedings of the IEEE Conference on Sensors (SENSORS'14), Valencia, Spain, 2–5 November 2014; pp. 424–427.
93. Imaeda, K.; Shibata, S.; Matsushima, M.; Kawabe, T.; Shikida, M. Responsible time shorting of flexible thermal flow sensor for medical applications. In Proceedings of the IEEE Conference on Sensors (SENSORS'15), Busan, South Korea, 1–4 November 2015; pp. 1–4.
94. Miao, J.; Leu, T.; Yu, J.; Tu, J.; Wang, C.; Lebiga, V.; Mironov, D.; Pak, A.; Zinovyev, V.; Chung, K. MemS thermal film sensors for unsteady flow measurement. *Sens. Actuators A Phys.* **2015**, *235*, 1–13. [[CrossRef](#)]
95. Wu, S.; Lin, Q.; Yuen, Y.; Tai, Y.-C. MEMS flow sensors for nano-fluidic applications. *Sens. Actuators A Phys.* **2001**, *89*, 152–158. [[CrossRef](#)]
96. Chen, J.; Fan, Z.; Zou, J.; Engel, J.; Liu, C. Two-dimensional micromachined flow sensor array for fluid mechanics studies. *J. Aerosp. Eng.* **2003**, *16*, 85–97. [[CrossRef](#)]
97. Miao, J.-J.; Tu, J.; Chou, J.; Lee, G. Sensing flow separation on a circular cylinder by micro-electrical-mechanical-system thermal-film sensors. *AIAA J.* **2006**, *44*, 2224–2230. [[CrossRef](#)]
98. Liu, K.; Yuan, W.; Deng, J.; Ma, B.; Jiang, C. Detecting boundary-layer separation point with a micro shear stress sensor array. *Sens. Actuators A Phys.* **2007**, *139*, 31–35. [[CrossRef](#)]
99. Tung, S.; Rokadia, H.; Li, W.J. A micro shear stress sensor based on laterally aligned carbon nanotubes. *Sens. Actuators A Phys.* **2007**, *133*, 431–438. [[CrossRef](#)]
100. Tan, Z.; Shikida, M.; Hirota, M.; Xing, Y.; Sato, K.; Iwasaki, T.; Iriye, Y. Characteristics of on-wall in-tube flexible thermal flow sensor under radially asymmetric flow condition. *Sens. Actuators A Phys.* **2007**, *138*, 87–96. [[CrossRef](#)]
101. Yu, H.; Ai, L.; Rouhanizadeh, M.; Hamilton, R.; Hwang, J.; Meng, E.; Kim, E.S.; Hsiai, T.K. Polymer-based cardiovascular shear stress sensors. In Proceedings of the 2nd ASME Conference on Frontiers in Biomedical Devices, Irvine, CA, USA, 7–8 June 2007; pp. 29–30.
102. Qu, Y.; Chow, W.W.; Ouyang, M.; Tung, S.C.; Li, W.J.; Han, X. Ultra-low-powered aqueous shear stress sensors based on bulk EG-CNTs integrated in microfluidic systems. *IEEE Trans. Nanotechnol.* **2008**, *7*, 565–572.
103. Chang, L.-Y.; Li, P.-Y.; Zhao, L.; Hoang, T.; Meng, E. Integrated flow sensing for focal biochemical stimulation. In Proceedings of the 3rd IEEE International Conference on Nano/Micro Engineered and Molecular Systems, Sanya, China, 6–9 January 2008.
104. Li, C.; Wu, P.-M.; Han, J.; Ahn, C.H. A flexible polymer tube lab-chip integrated with microsensors for smart microcatheter. *Biomed. Microdevices* **2008**, *10*, 671–679. [[CrossRef](#)]

105. Wiegerink, R.; Lammerink, T.; Dijkstra, M.; Haneveld, J. Thermal and Coriolis type micro flow sensors based on surface channel technology. *Procedia Chem.* **2009**, *1*, 1455–1458. [[CrossRef](#)]
106. Liu, P.; Zhu, R.; Que, R. A flexible flow sensor system and its characteristics for fluid mechanics measurements. *Sensors* **2009**, *9*, 9533–9543. [[CrossRef](#)] [[PubMed](#)]
107. Kielbasa, J. Measurement of gas flow velocity: Anemometer with a vibrating hot wire. *Rev. Sci. Instrum.* **2010**, *81*, 015101. [[CrossRef](#)]
108. Ito, Y.; Higuchi, T.; Takahashi, K. Submicroscale flow sensor employing suspended hot film with carbon nanotube fins. *J. Therm. Sci. Technol.* **2010**, *5*, 51–60. [[CrossRef](#)]
109. Bailey, S.C.; Kunkel, G.J.; Hultmark, M.; Vallikivi, M.; Hill, J.P.; Meyer, K.A.; Tsay, C.; Arnold, C.B.; Smits, A.J. Turbulence measurements using a nanoscale thermal anemometry probe. *J. Fluid Mech.* **2010**, *663*, 160–179. [[CrossRef](#)]
110. Kuo, J.T.; Chang, L.-Y.; Li, P.-Y.; Hoang, T.; Meng, E. A microfluidic platform with integrated flow sensing for focal chemical stimulation of cells and tissue. *Sens. Actuators B Chem.* **2011**, *152*, 267–276. [[CrossRef](#)]
111. Que, R.; Zhu, R. Aircraft aerodynamic parameter detection using micro hot-film flow sensor array and BP neural network identification. *Sensors* **2012**, *12*, 10920–10929. [[CrossRef](#)] [[PubMed](#)]
112. Sun, J.; Cui, D.; Zhang, L.; Chen, X.; Cai, H.; Li, H. Fabrication and characterization of a double-heater based MEMS thermal flow sensor. *Sens. Actuators A Phys.* **2013**, *193*, 25–29. [[CrossRef](#)]
113. Miao, Z.; Chao, C.Y.; Chiu, Y.; Lin, C.-W.; Lee, Y.-K. Design and fabrication of micro hot-wire flow sensor using 0.35 μm CMOS MEMS technology. In Proceedings of the 9th IEEE International Conference on Nano/Micro Engineered and Molecular Systems (NEMS, 2014), Waikiki Beach, HI, USA, 13–16 April 2014; pp. 289–293.
114. Hasegawa, Y.; Yamada, T.; Shikida, M. Fabrication of smooth-surfaced flexible thermal sensor for detecting wall shear stress. In Proceedings of the 29th IEEE International Conference on Micro Electro Mechanical Systems (MEMS'16), Shanghai, China, 24–28 January 2016; pp. 1010–1013.
115. Yu, J.-M.; Leu, T.-S.; Miao, J.-J.; Chen, S.-J. MEMS flexible thermal flow sensor for measurement of boundary layer separation. *Mod. Phys. Lett. B* **2016**, *30*, 1650177. [[CrossRef](#)]
116. Ghouila-Houri, C.; Gerbedoen, J.-C.; Claudel, J.; Gallas, Q.; Garnier, E.; Merlen, A.; Viard, R.; Talbi, A.; Pernod, P. Wall shear stress and flow direction thermal MEMS sensor for separation detection and flow control applications. *Procedia Eng.* **2016**, *168*, 774–777. [[CrossRef](#)]
117. Yu, H.; Ai, L.; Rouhanizadeh, M.; Patel, D.; Kim, E.S.; Hsiai, T.K. Flexible polymer sensors for in vivo intravascular shear stress analysis. *J. Microelectromech. Syst.* **2008**, *17*, 1178–1186.
118. Gardner, J.W.; Varadan, V.K. *Microsensors, MEMS and Smart Devices*; John Wiley & Sons, Inc.: Hoboken, NJ, USA, 2001.
119. Uma, S.; McConnell, A.; Asheghi, M.; Kurabayashi, K.; Goodson, K. Temperature-dependent thermal conductivity of undoped polycrystalline silicon layers. *Int. J. Thermophys.* **2001**, *22*, 605–616. [[CrossRef](#)]
120. Assael, M.; Antoniadis, K.; Wu, J. New measurements of the thermal conductivity of PMMA, BK7, and Pyrex 7740 up to 450K. *Int. J. Thermophys.* **2008**, *29*, 1257–1266. [[CrossRef](#)]
121. Petropoulos, A.; Goustouridis, D.; Speliotes, T.; Kaltsas, G. Demonstration of a new technology which allows direct sensor integration on flexible substrates. *Eur. Phys. J. Appl. Phys.* **2009**, *46*, 12507. [[CrossRef](#)]
122. Shin, Y.S.; Cho, K.; Lim, S.H.; Chung, S.; Park, S.-J.; Chung, C.; Han, D.-C.; Chang, J.K. PDMS-based micro PCR chip with parylene coating. *J. Micromech. Microeng.* **2003**, *13*, 768. [[CrossRef](#)]
123. Xu, Y.; Chiu, C.-W.; Jiang, F.; Lin, Q.; Tai, Y.-C. A MEMS multi-sensor chip for gas flow sensing. *Sens. Actuators A Phys.* **2005**, *121*, 253–261. [[CrossRef](#)]
124. Xu, Y.; Lin, Q.; Lin, G.; Katragadda, R.B.; Jiang, F.; Tung, S.; Tai, Y.-C. Micromachined thermal shear-stress sensor for underwater applications. *J. Microelectromech. Syst.* **2005**, *14*, 1023–1030.
125. Haneef, I.; Ali, S.Z.; Udrea, F.; Coull, J.D.; Hodson, H.P. High performance SOI-CMOS wall shear stress sensors. In Proceedings of the IEEE Conference on Sensors, Atlanta, GA, USA, 28–31 October 2007; pp. 1060–1064.
126. Haneef, I.; Coull, J.D.; Ali, S.Z.; Udrea, F.; Hodson, H.P. Laminar to turbulent flow transition measurements using an array of SOI-CMOS MEMS wall shear stress sensors. In Proceedings of the IEEE Sensors, Lecce, Italy, 26–29 October 2008; pp. 57–61.
127. Ernst, H.; Jachimowicz, A.; Urban, G.A. High resolution flow characterization in Bio-MEMS. *Sens. Actuators A Phys.* **2002**, *100*, 54–62. [[CrossRef](#)]

128. Won, S.S.; Kawahara, M.; Glinsek, S.; Lee, J.; Kim, Y.; Jeong, C.K.; Kingon, A.I.; Kim, S.-H. Flexible vibrational energy harvesting devices using strain-engineered perovskite piezoelectric thin films. *Nano Energy* **2019**, *55*, 182–192. [[CrossRef](#)]
129. Orrego, S.; Shoole, K.; Ruas, A.; Doran, K.; Caggiano, B.; Mittal, R.; Kang, S.H. Harvesting ambient wind energy with an inverted piezoelectric flag. *Appl. Energy* **2017**, *194*, 212–222. [[CrossRef](#)]
130. Mansoor, M.; Haneef, I.; Akhtar, S.; Rafiq, M.A.; De Luca, A.; Ali, S.Z.; Udrea, F. An SOI CMOS-Based Multi-Sensor MEMS Chip for Fluidic Applications. *Sensors* **2016**, *16*, 1608. [[CrossRef](#)]
131. Haneef, I.; Hodson, H.P.; Miller, R.; Udrea, F. Shear Stress Sensors. U.S. Patent 9080907 B2, 14 July 2015.
132. Udrea, F.; Gardner, J.; Setiadi, D.; Covington, J.; Dogaru, T.; Lu, C.; Milne, W. Design and simulations of SOI CMOS micro-hotplate gas sensors. *Sens. Actuators B Chem.* **2001**, *78*, 180–190. [[CrossRef](#)]
133. Mansoor, M.; Haneef, I.; Akhtar, S.; Rafiq, M.; Ali, S.; Udrea, F. SOI CMOS multi-sensors MEMS chip for aerospace applications. In Proceedings of the IEEE Conference on Sensors, Valencia, Spain, 2–5 November 2014; pp. 1204–1207.
134. Lai, S.; Johnson, D.; Westerman, R. Aspect ratio dependent etching lag reduction in deep silicon etch processes. *J. Vac. Sci. Technol. A Vac. Surf. Films* **2006**, *24*, 1283–1288. [[CrossRef](#)]
135. Yeom, J.; Wu, Y.; Shannon, M.A. Critical aspect ratio dependence in deep reactive ion etching of silicon. In Proceedings of the 12th International Conference on Solid-State Sensors, Actuators and Microsystems (TRANSDUCERS'03), Boston, MA, USA, 8–12 June 2003; pp. 1631–1634.
136. Kleiner, M.B.; Kuhn, S.A.; Weber, W. Thermal conductivity measurements of thin silicon dioxide films in integrated circuits. *IEEE Trans. Electron Devices* **1996**, *43*, 1602–1609. [[CrossRef](#)]
137. Berns, A.; Buder, U.; Obermeier, E.; Wolter, A.; Leder, A. AeroMEMS sensor array for high-resolution wall pressure measurements. *Sens. Actuators A Phys.* **2006**, *132*, 104–111. [[CrossRef](#)]



© 2019 by the authors. Licensee MDPI, Basel, Switzerland. This article is an open access article distributed under the terms and conditions of the Creative Commons Attribution (CC BY) license (<http://creativecommons.org/licenses/by/4.0/>).